Thermochimica Acta 683 (2020) 178437

Contents lists available at ScienceDirect

Thermochimica Acta

journal homepage: www.elsevier.com/locate/tca

A study of the kinetics of bismuth telluride synthesis by an oxide reduction method

Bartosz Trawiński*, Beata Bochentyn, Marcin Łapiński, Bogusław Kusz

Gdańsk University of Technology, Faculty of Applied Physics and Mathematics, Solid State Physics Department, ul. G. Narutowicza 11/12, 80-233 Gdańsk, Poland

ARTICLE INFO

Keywords:
Bismuth telluride
Oxide reduction
Reaction kinetics
Autocatalysis

ABSTRACT

The kinetics of a reduction of bismuth and tellurium oxides in a hydrogen atmosphere, leading to the formation of thermoelectric bismuth telluride is investigated. The evaluation of the reaction kinetics was based on a thermogravimetric analysis performed in non-isothermal conditions. A non-parametric analysis method and the Friedman method were used for the evaluation of the data. Additionally, for a better understanding of the process, reactions of the reduction of Bi_2O_3, TeO_2 as well as $Bi_2Te_2O_7$ and $Bi_2Te_4O_{11}$, which are formed as intermediate products, were investigated. The activation energies calculated for the reactions were between 56 kJ/mol in the case of the $Bi_2Te_2O_7$ reduction and 100 kJ/mol for the reduction of mixed oxides. No correlation between the activation energy and the Bi:Te ratio in the reduced material was found. The calculated conversion functions also differed between the investigated reactions. A self-heating process was found for TeO_2 and $Bi_2Te_4O_{11}$ reduction reactions. In the case of the tellurium oxide, it was assigned to the melting of Te nanoparticles. These effects were also found to enhance the synthesis of Bi_2Te_3 by the reduction of mixed bismuth and tellurium oxides. The resulting thermoelectric material was found to be completely reduced, with no traces of oxygen inthe XPS spectrum. EDX mapping of the cross-section of material's grains revealed a homogenous distribution of elements in the final product.

1. Introduction

The reduction of metal oxide in reducing atmosphere, typically hydrogen or carbon monoxide, can be used as a method of a production of metals and different intermetallic compounds and composites, *e.g.* Fe-Ni-Co alloys [1–4], Cu-W composites [5], Co-W and Co-Mo alloys [6], W-Ag alloys [7], Ag-Mo composites [8]. The reduction of two or more oxides together can be performed at a lower temperature than the reduction of single oxide [8]. Tuning the temperature of the process allows for the formation of metal-oxide composites [8] or changing the oxidation states in a system with mixed valence states of elements [9].

It is worth mentioning, that not only the reduction by gaseous agents is investigated. The results of the kinetic analysis of processes using solid reagents have also been published, *e.g.* [10]. Interestingly, conclusions about the reduction of iron oxide presented therein are in agreement with those obtained for the reduction with carbon monoxide in [11]. Similar mechanisms were found to be limiting the reaction – initially the surface reaction and diffusion through the product layer during further process. The calculated activation energies were also in good agreement. In thermite-type reactions, metals are used as reducing agents in high temperature processes. A huge amount of released heat makes these reactions self-propagating [12].

The oxide reduction method has been used to synthesize bismuth telluride-based materials by several research groups [13–20]. An oxide material for the reduction can be prepared *e.g.* by co-precipitation of oxides [13–15], allowing for a synthesis of nanostructured material [15]. Kim et al. [21] found, that the treatment of $Bi_2(Te,Se)_3$ with hydrogen after mechanical alloying decreases the amount of oxygen in the material and enhances its thermoelectric properties.

In order to understand the mechanisms of the chemical reaction, in this case a reduction of oxides leading to the formation of bismuth telluride, evaluation of its kinetics is necessary. The kinetics of chemical reactions is expressed by an equation for the rate r of the reaction, which is a change of reaction extent α (hereinafter also referred to as conversion) in time – Eq. (1) [22].

$$r = \frac{d\alpha}{dt} = k \cdot f(\alpha, T) \tag{1}$$

In Eq. (1) T is temperature, f is a function depending on the processes limiting the rate of the reaction and k is the rate constant. The rate constant is described by Eq. (2), where A is the frequency factor, E is the activation energy and R is the gas constant.

* Corresponding author.
E-mail address: bartosz.trawinski@pg.edu.pl (B. Trawiński).

https://doi.org/10.1016/j.tca.2019.178437
Received 25 June 2019; Received in revised form 16 October 2019; Accepted 19 October 2019
Available online 24 October 2019

$$k = A \bullet \exp\left(\frac{-E(\alpha, T)}{RT}\right) \quad (2)$$

The mechanisms and the kinetics of the reduction of metal oxides with hydrogen have been investigated since the 19th century, see [23] and the references therein. Thermogravimetric analysis is often used for the investigation of these reactions [5]. A complete analysis requires evaluation of *A*, *E,* and *f* from Eqs. (1) and (2). Function *f* can be fit to a set of different models derived for different mechanisms limiting the reaction rate [24]. These functions are calculated with simple geometrical models of the reactants' particles [25] or other simplifying (such as one nucleus of new phase per each grain) [26] assumptions, or even reaction order models, relevant for homogenous reactions. Using the fitting procedure only is not sufficient for the description of the phenomena driving the reaction. Additional analysis of the structure of the investigated material can provide insight into the complexity of the reaction mechanisms, *e.g.* in [27] a hierarchical structure of the reacting material was found.

The Kinetics of the reduction of mixed bismuth and tellurium oxides hasn't been investigated yet. Moreover, no research considering the reaction of only TeO_2 with hydrogen was performed. In this study, the kinetics of bismuth telluride synthesis by bismuth and tellurium mixed oxides reduction in hydrogen is investigated. For a better understanding of the process, a similar analysis of the reduction of both bismuth and tellurium oxide, as well as double bismuth tellurium oxides ($Bi_2Te_2O_7$ and $Bi_2Te_4O_{11}$), is performed. In order to compare the reduction of the mixture with the reduction of single oxides, a thermogravimetric analysis of a bismuth oxide powder in a hydrogen atmosphere was also performed. This reaction has previously been investigated [28–30]. In order to obtain data for the comparison, measurements were performed with the Bi_2O_3 powder used in this study. The results are presented in Supplementary Information, Figs. S9–S12.

2. Material and methods

2.1. Experimental

The different oxide materials used in this study were crystalline with submicrometre grain size. The materials used as substrates of the investigated reactions were commercial Bi_2O_3 (ACROS 99.9%) and TeO_2 (ACROS 99 + %). The oxides were milled in a planetary mill with 600 rpm rotation speed for 20 h. Fritzch Pulverisette 7 with zirconia bowls and zirconia balls with a 3 mm diameter were used (ball/powder ratio *ca.* 5:1). Isopropyl alcohol was added to the powders. In order to investigate the reduction of mixed bismuth and tellurium oxides, the milled powders were mixed in a 1:3 (Bi_2O_3:TeO_2) molar ratio in a planetary mill, with a significantly lower speed (100 rpm) in order to avoid further decreasing of grains' size. $Bi_2Te_2O_7$ and $Bi_2Te_4O_{11}$ double oxides were separately synthesised *via* solid state reaction, at 450 and 500 °C respectively, from the single oxides, and ball-milled using the procedure described above. Additionally, a mixture of $Bi_2Te_2O_7$ and $Bi_2Te_4O_{11}$ (1:1 M ratio) was prepared by melting bismuth and tellurium oxides at 950 °C in the open air in order to provide good dispersion. The material was also milled with the same procedure as the other oxide materials.

SEM images of all oxide materials used in this study are presented in Supplementary information, Figs. S1–S3, S5, and S7. Additionally, for double oxides, XRD patterns are provided (Figs. S4, S6).

The kinetics of the reactions was investigated with thermogravimetric analysis in a hydrogen (99.999%) atmosphere, under a 160 cm^3/min flow rate, using a self-made apparatus, described in our previous paper [30]. The TGA measurements of the reduction of TeO_2 and a mixture of Bi_2O_3 and TeO_2 were performed in non-isothermal conditions, with constant heating rates 2–6 K/min. Measurements were performed every 5 s. Additionally, in order to evaluate the structure of the material at different stages of the reaction, the process was interrupted at particular moments by rapid cooling and gas exchange to nitrogen.

The phase composition of the fabricated materials was investigated by using the X-ray diffraction method (XRD) using an X'Pert Pro MPD Philips diffractometer with Cu Kα (1.542 Å) radiation at room temperature. The measurements were performed in a 2Θ range of 20-70° with a 0.025° step and 1 s step time. The morphology of the fabricated materials was observed using an FEI Quanta FEG 250 Scanning Electron Microscope (SEM) with a secondary electrons detector. Elemental analysis was performed with energy dispersive X-ray spectroscopy using an EDAX Genesis APEX 2i with the ApolloX SDD spectrometer. X-ray photoemission spectroscopy (XPS) analysis was performed in a multi-chamber ultrahigh vacuum system (Omicron nanoTechnology), at room temperature under a pressure below 1.1×10^{-9} mBar. The photoelectrons were excited by an Mg-Kα X-Ray anode operated at 15 keV and 300 W. An Omicron Argus hemispherical electron analyser with a round aperture of 4 mm was used for the analysis of the emitted photoelectrons. Measurements were carried out in a constant analyser energy (CAE) mode with pass energy equal to 50 eV. The binding energies were corrected using the background C1s line (285.0 eV) as a reference. The XPS spectra were analysed using a Shirley background subtraction and Gaussian-Lorentzian curve. To remove contaminations and oxides, the surface was etched with Ar ions before the measurement.

The reaction extent α values were calculated on the basis of TGA results according to Eq. (3), where m_0 is the initial mass of the material, m is the measured mass and m_{ox} is the mass of the oxygen atoms in the starting material.

$$\alpha = \frac{m_0 - m}{m_{ox}} \quad (3)$$

The obtained α values were smoothed using a moving average with a window of 15 measurement points. An example of raw and smoothed data is presented in Supplementary Information, Fig. S8. The TGA data are presented in Supplementary Information, in the sections regarding particular reactions, Figs, S9, S13, S15, S19, S22, S23.

2.2. Kinetic data analysis methods

Considering a reaction which can be described with Eqs. (1) and (2), the assumption that *E* and *f* are dependent only on α can be made. Then, the Arrhenius relation can be used to calculate the values of the activation energy for different reaction extent values. Eq. (1), with *k* taken from Eq. (2), is logarithmised, leading to Eq. (4).

$$\ln r = \frac{-E(\alpha)}{RT} + \ln[A \bullet f(\alpha)] \quad (4)$$

Taking measurement data from several measurements in different thermal conditions, the activation energy for any given α can be calculated from the slope of the linear dependence of ln*r* on 1/*T* (taking *r* and *T* measured at the same moment when the given α). This procedure, known as the isoconversional Friedman method, was performed with Kinetics2015 software. The Friedman method was selected because it allows for a calculation of the activation energy at different stages of the investigated process (if the assumptions are fulfilled). It also directly uses basic kinetic Eqs. (1) and (2).

Another data analysis method used in this study is based on the assumption, that the reaction rate can be described by independent functions *f(α)* and *h(T)*, the latter describing the dependence of the reaction rate on the temperature, according to Eq. (5).

$$r = f(\alpha) \bullet h(T) \quad (5)$$

In the case of *n* parallel reactions, Eq. (5) has the form of Eq. (6).

$$r = \sum_n [f_n(\alpha) \bullet h_n(T)] \quad (6)$$

Following this assumption, a matrix **R** consisting of the r_{pq} values of the reaction rates is constructed. Indexes *p* and *q* correspond to different *α* and *T* values. Performing singular value decomposition (SVD) on the matrix **R** returns a number (n) of $\mathbf{u_n}$, s_n, and $\mathbf{v_n}^T$ sets, fulfilling Eq. (7).

$$r_{pq} = \sum_n (\boldsymbol{u_n}_p \bullet s_n \bullet \boldsymbol{v_n}^T_q) \tag{7}$$

When the kinetic data are considered and consecutive *p* and *q* indexes respectively correspond to consecutive *α* and *T* values, each set (n = 1, 2, ...) of $\mathbf{u_n}$, s_n, and $\mathbf{v_n}^T$ can be recalculated, according to Eqs. (8.1) and (8.2), resulting from Eqs. (6) and (7), into vectors $\mathbf{f_n}$ and $\mathbf{h_n}$, which are values of functions $f_n(\alpha)$ and $h_n(T)$.

$$\boldsymbol{f_n} = a_n \bullet \boldsymbol{u_n} \tag{8.1}$$

$$\boldsymbol{h_n} = \frac{s_n}{a_n} \bullet \boldsymbol{v_n} \tag{8.2}$$

a_n is an arbitrary number. This is a non-parametric method of kinetic analysis (NPK), as it returns values of functions rather than parameters of equations. A detailed description of this procedure can be found elsewhere [31]. Briefly, due to the fact, that the data from the 5 non-isothermal measurements do not cover the whole *α*-*T* plane, the range covered by the experimental values was divided into several overlapping submatrices. Consecutive *p* indexes were corresponding to values of *α* differing by 0.1% and *q* indexes to values of *T* differing by 0.1 K. The missing values of the submatrices were estimated by a cubic interpolation algorithm. In the case of all analyses performed in this work, only the first pair of vectors **f** and **h** from each submatrix was considered. For all analysed data sets, the second and next **h** vectors had both negative and positive values, which makes them have no physical meaning. The s_1 values were at least an order of magnitude higher than s_2 (in SVD always $s_n > s_{n+1}$). The results of the SVD procedure for each submatrix were normalised, by choosing appropriate values of *a* for each submatrix, in order to provide continuity of functions *f(α)* and *h(T)* in the whole ranges of the reaction extent and temperature.

3. Results and discussion

3.1. TeO_2 reduction

The reduction of tellurium oxide was investigated with thermogravimetric analysis with different constant heating rates. The results in a derivative form (reaction rate) are plotted against the reaction extent and temperature in Fig. 1 and Fig. 2 respectively. As can be seen in the Figures, the reaction consists of two overlapping parts. During the first one, the dependencies of the reaction rate on conversion are similar for different heating rates. Reaction rate changes are dependent on the reaction extent, so the isoconversional principle can be applied.

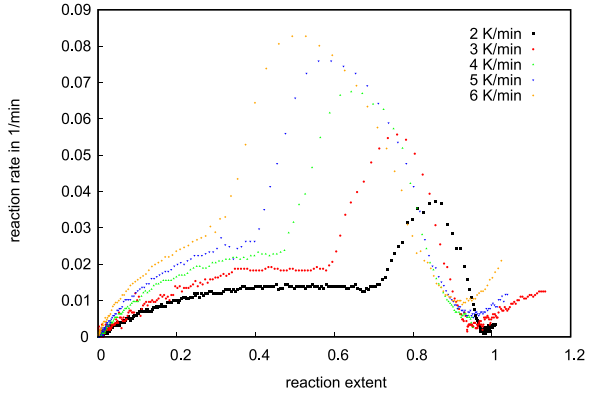

Fig. 1. Dependence of reaction rate on reaction extent during TeO_2 reduction with different heating rates.

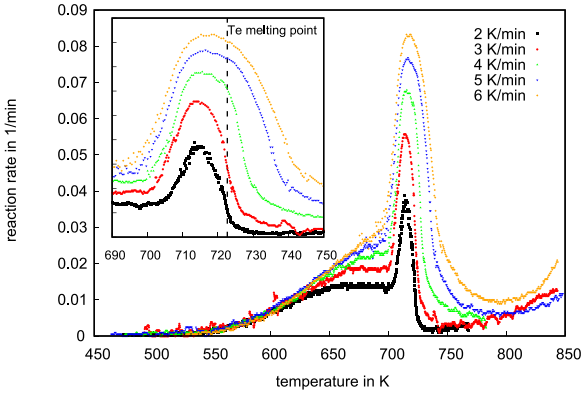

Fig. 2. Dependence of reaction rate on temperature during TeO_2 reduction with different heating rates (inset: high reaction rate range with marked tellurium melting point).

During the second part, starting at about a temperature of 700 K, changes in the rate are dependent on the temperature rather than on *α*. Moreover, this temperature-dependent process is interfering with liquid tellurium evaporation, manifesting itself in mass changes above 100% of the expected reaction, increasing with the temperature. The melting point of tellurium is equal to 723 K and, in this case, can be even lower due to the nanometric size of Te particles [32].

The calculated activation energy values are presented in Fig. 3. The obtained values can be considered as real below 32% of the conversion degree (where the second part of the reaction starts for 6 K/min heating rate). Above the 32% limit, the increase in the reaction rate (for a given *α* value) is observed firstly for higher temperature (higher heating rate) measurements. Consequently, the Arrhenius relation returns higher values of *E*. A further decrease, starting at 67% of conversion, is related to the fact, that for high reaction extent values, calculated according to Eq. (3), the mass changes result from evaporation only at high temperatures (high heating rates), while for low temperatures the reduction is still proceeding and the mass changes are faster.

Non-parametric analysis was also performed, in order to obtain the conversion function *f*. Moreover, this method of analysis does not use the dependence on the reaction extent, as the Friedman method does. Therefore, the non-parametric method is useful for processes in which changes of mechanisms are dependent on temperature rather than on the conversion, according to the Eq. (5). The calculated thermal function *h(T)* will ideally show a change in the activation energy at the temperature of the mechanism change. The obtained values of *h(T)* and *f(α)* are presented in Fig. 4 and Fig. 5. The thermal function shows activation behaviour up to the temperature of 700 K, corresponding to the upturn in the reaction rate. The calculated activation energy value

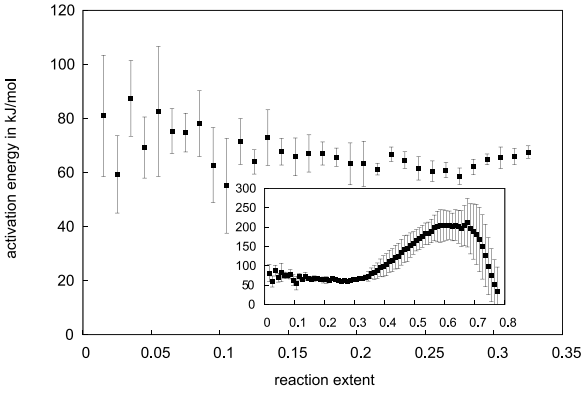

Fig. 3. Dependence of activation energy calculated with Arrhenius method on reaction extent during TeO_2 reduction with different heating rates (main plot: range of isoconversional principle applicability, inset: whole range).

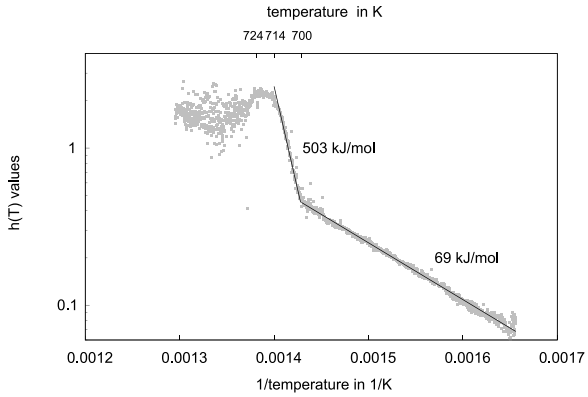

Fig. 4. Thermal function obtained from nonparametric kinetic analysis of the TeO_2 reduction data.

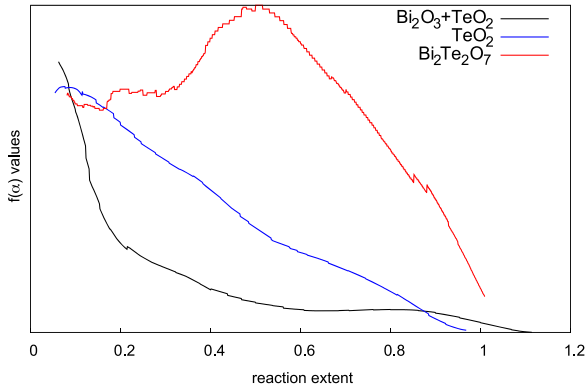

Fig. 5. Values of the conversion function resulting from non-parametric kinetic analysis of the reduction data of different materials.

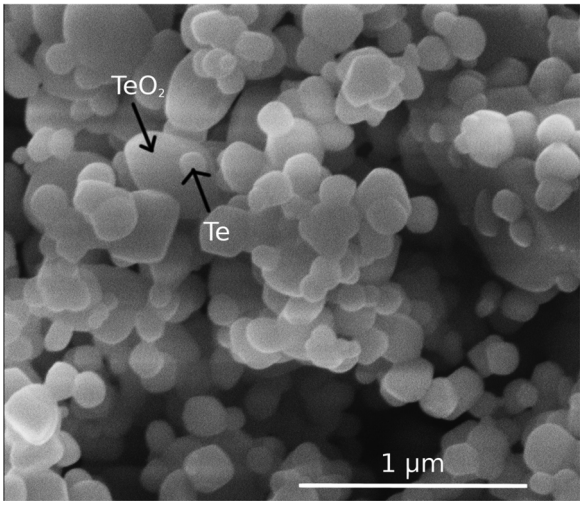

Fig. 6. Partially reduced TeO_2 (up to 680 K, 6 K/min) with visible nanometric Te particles.

of (69.2 ± 0.2) kJ/mol is in agreement with the isoconversional analysis results. In the case of non-parametric calculations, the uncertainty of the activation energy is calculated on the basis of a deviation of a linear regression parameter.

Above a temperature of 700 K, the slope of the Arrhenius plot corresponds to the activation energy as high as 503 kJ/mol. This is an unexpected result, considering the significant increase in the reaction rate. The effect of the increased value of the function *h* can be a consequence of a rapid release of heat in an exothermal reaction – enthalpy

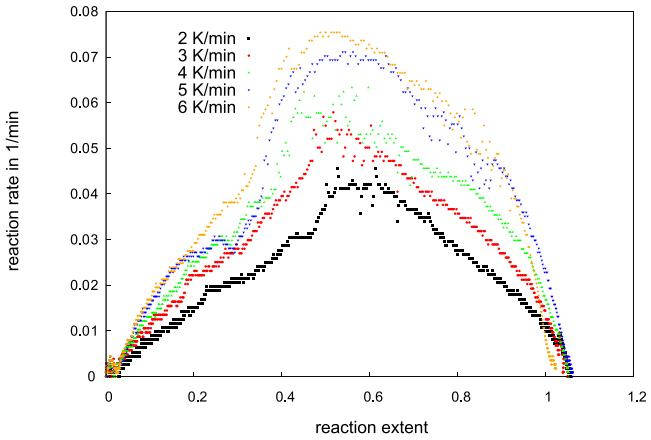

Fig. 7. Dependence of reaction rate on reaction extent during $Bi_2Te_2O_7$ reduction.

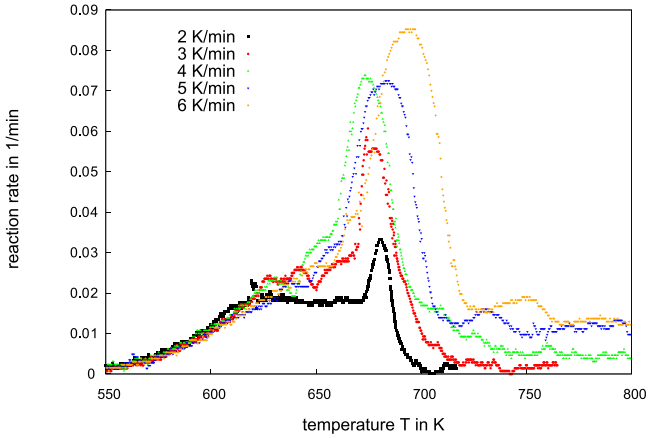

Fig. 8. Dependence of the reaction rate on temperature during the reduction of $Bi_2Te_4O_{11}$.

at 700 K ΔH = -201 kJ/mol (liquid product) and ΔH = -218 kJ/mol (solid product) - resulting in locally increased temperature.

Calculated values of function *f(α)* are presented in Fig. 5 (blue curve). These values nearly form a straight line, so the first order reaction equation can be used to describe the dependence.

The temperature, in which the upturn in the reaction rate occurs, varies between measurements, from 696 K (6 K/min) to 704 K (2 K/min). This correlation between the characteristic temperature and heating rate, suggests, that the variation of the upturn temperature is a result of a delay of its measurement, resulting from the measurement being done below the crucible. The effect is not related to the mechanisms and kinetics of the process. Another slight enhancement is also visible close to the tellurium melting point, 723 K, see inset in Fig. 3. In order to explain the phenomenon of the rapid increase in reaction rate at about 700 K, two reactions were performed and interrupted at 670 (heating rate 2 K/min) and 720 K (6 K/min). XRD measurements performed on these materials showed only the presence of Te and TeO_2 phases. The XRD patterns are provided in Supplementary Information, Fig. S14. SEM images of partially reduced powder are presented in Fig. 6. Small particles with a 50–200 nm diameter range are visible. EDX point analysis of the smaller particles revealed a high Te:O atomic ratio, in the range of 3.5 – 3.8. When the beam was focused on large particles, that ratio was equal to 1.2 – 2.2. Considering the large volume of the material measured with this technique, the smaller particles can be identified as tellurium. The calculated melting point of such particles is close to 700 K [32]. Therefore, the increase in the reaction rate can be explained by the enhanced catalytic activity of liquid

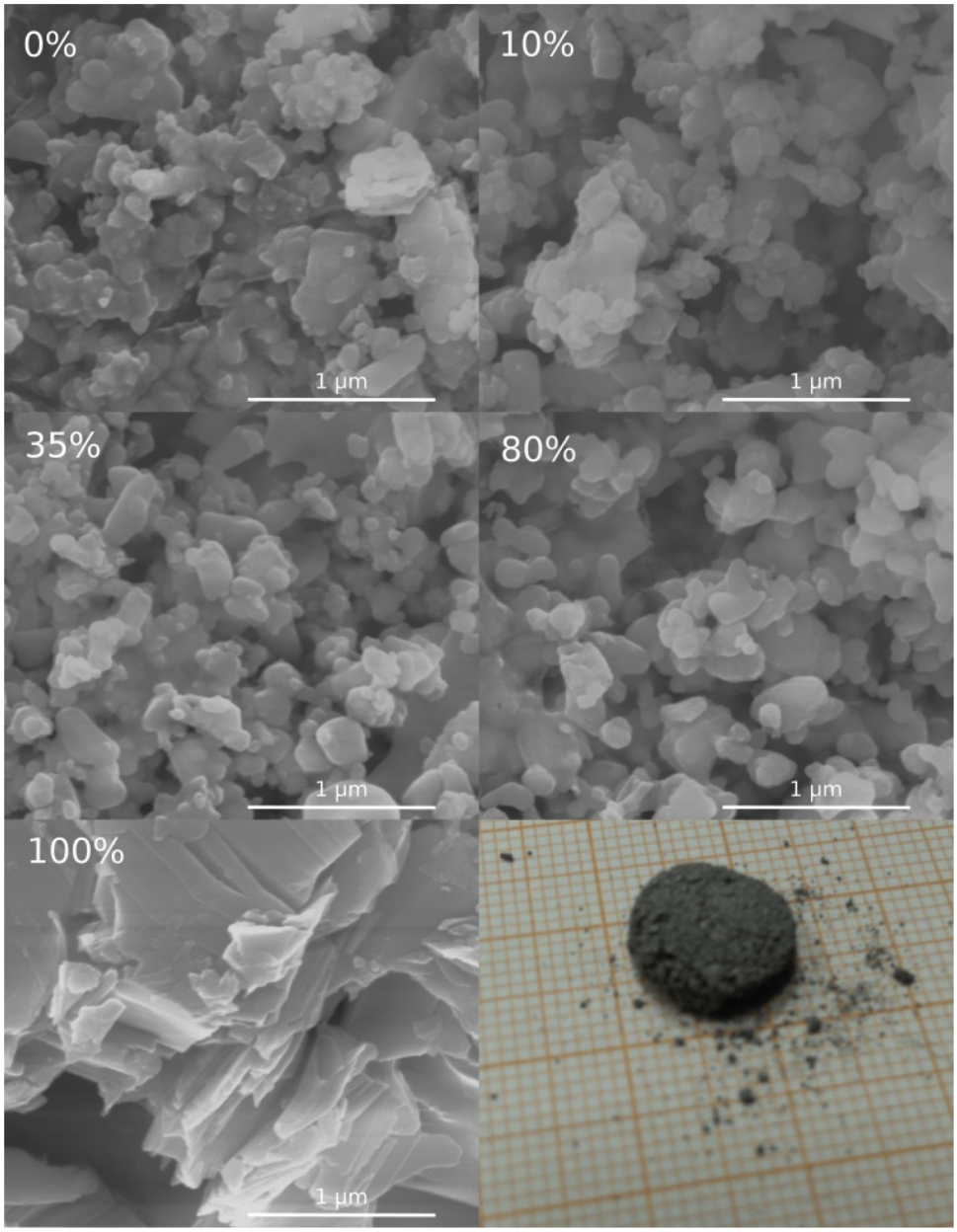

Fig. 9. SEM images of material reduced at 4 K/min heating rate at different stages of the reaction (bottom right: a photograph of the material after the completed reaction).

tellurium or the faster diffusion of the gaseous species through the liquid tellurium phase, comparing to the solid phase. This increase in the reaction rate leads to faster heat release and initiates a self-propagating process. The abovementioned heat of the reaction (per one mole) is equal to the heat necessary to heat one mole of Te plus one mole of TeO_2 to the temperature of about 2000 K (thermodynamic data from HCS Chemistry 9 package). Therefore, the reaction can be considered as self-propagating because the requirement for the adiabatic temperature [33] is fulfilled.

3.2. Reduction of bismuth and tellurium double oxides

In the Bi-Te-O system, double oxides ($Bi_2Te_2O_7$ and $Bi_2Te_4O_{11}$) are easily formed [34]. These phases were identified during the reduction of mixed Bi_2O_3 and TeO_2 oxides. Therefore, the reduction of double oxides was investigated.

The dependence of the reaction rate of $Bi_2Te_2O_7$ reduction on the reaction extent, presented in Fig. 7, shows a similar character for different heating rates. The temperature dependence of the reaction rate is available in the Supplementary Information, Fig. S16.

The activation energy, calculated with the non-parametric method, was found to be constant through almost the whole temperature and conversion range with a value of (55.9 ± 0.4) kJ/mol. Only at the beginning of the process, for α below 0.2, the energy was higher, indicating an autocatalytic mechanism. A plot of the h(T) function as well as the results of the isoconversional analysis, which are in a good agreement, can be found in Supplementary Information (Figs. S17 and S18). The lack of any characteristic temperature, at which a significant change of a course of the reaction occurs (such as for TeO_2), indicates that, in the experimental thermal conditions, the reaction mechanisms are dependent on the reaction extent rather than the temperature. Conversion function $f(\alpha)$ derived from non-parametric analysis, plotted in Fig. 5 (red curve), also shows different behaviour at the beginning of the reaction. A small upturn occurring at about 20% conversion is a

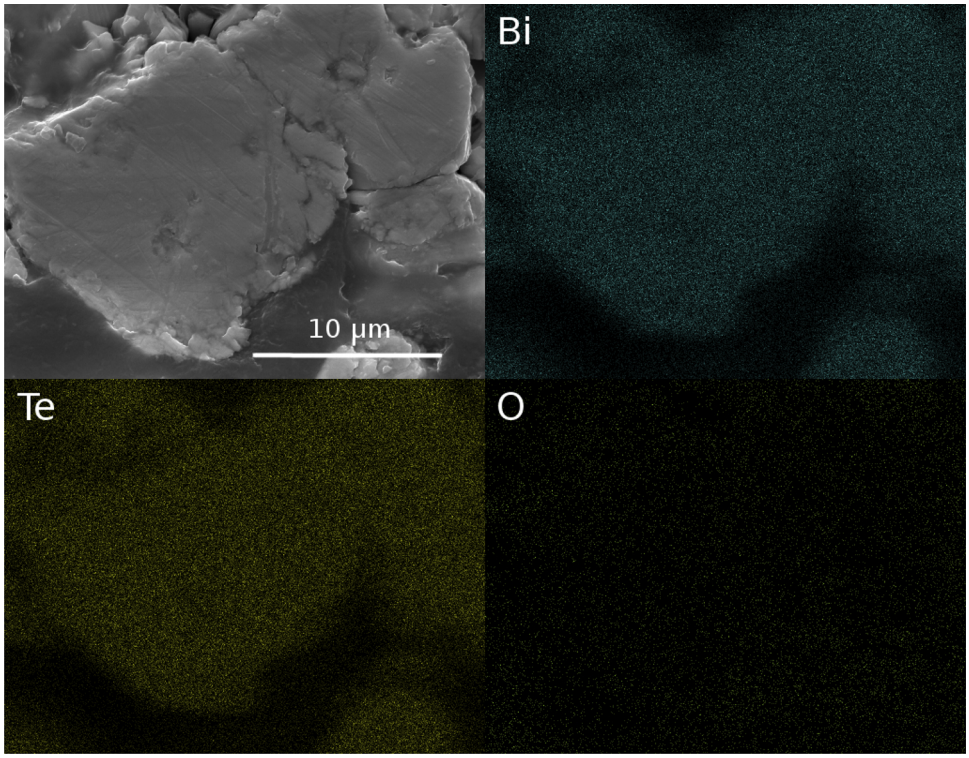

Fig. 10. SEM image of the cross-section of bismuth telluride grains embedded in epoxy resin; results of the elemental analysis of the same area performed by the EDX method.

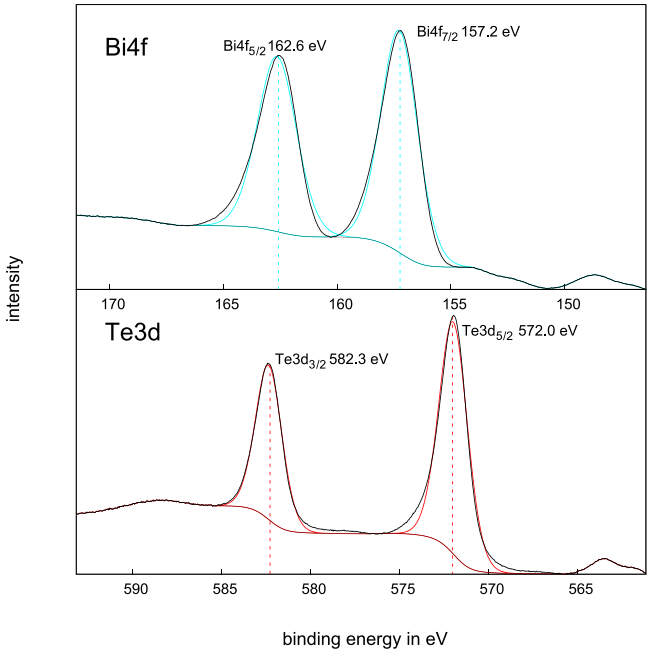

Fig. 11. XPS spectrum of bismuth telluride synthesized by the reduction in hydrogen with 4 K/min heating rate - Bi4f and Te3d regions.

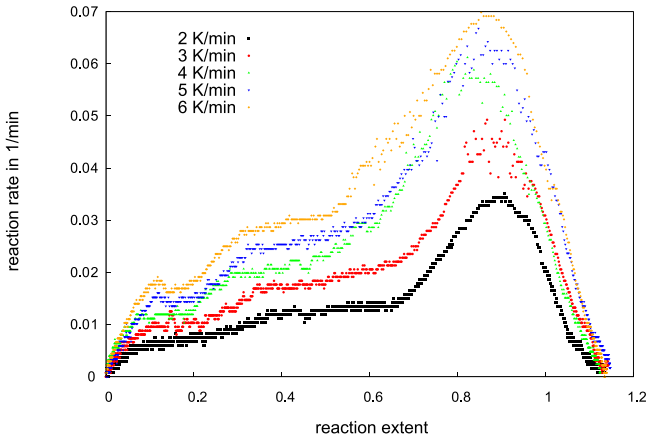

Fig. 12. Dependence of reaction rate on reaction extent during mixed Bi_2O_3 and TeO_2 reduction with different heating rates.

result of imperfect matching of the results of the SVD of the submatrices. The second part has a maximum at around 50% of the reaction extent. This is typical for Avrami-Erofev functions derived for nucleation-growth controlled reactions [22].

The rate of the $Bi_2Te_4O_{11}$ reduction shows a strong dependence on the temperature, presented in Fig. 8. The first local maximum of the reaction rate arises between 620 and 650 K. The comparison of different reactions with similar heating rates (Figs. S27–S31 in the Supplementary Information) shows that the first reaction rate maximum is nearly at the same temperature as that of the $Bi_2Te_2O_7$ reduction, especially for low heating rates. $Bi_2Te_4O_{11}$ forms a layered structure consisting of $Bi_2Te_2O_7$ layers and tellurium oxide layers [35,36]. It can be concluded, that the reduction of $Bi_2Te_4O_{11}$ is initially the reaction of the $Bi_2Te_2O_7$ substructure in the lattice. The onset temperature of the main maximum is between 658 and 672 K. There is no correlation between this temperature and the heating rate.

Non-parametric analysis of the $Bi_2Te_4O_{11}$ reduction data returned thermal function *h(T)* similar to that from the TeO_2 reduction. The result is provided in Supplementary Information, Fig. S20. For the slower part of the reaction, the Arrhenius course (linear plot in ln*rvs* 1/*T* coordinates) was found. For the second part, the values seemed to be overestimated. The activation energy calculated for the first part of the process was equal to (57.0 ± 0.6) kJ/mol, close to that of $Bi_2Te_2O_7$ reduction. Additionally, in this part of the reaction, the results obtained

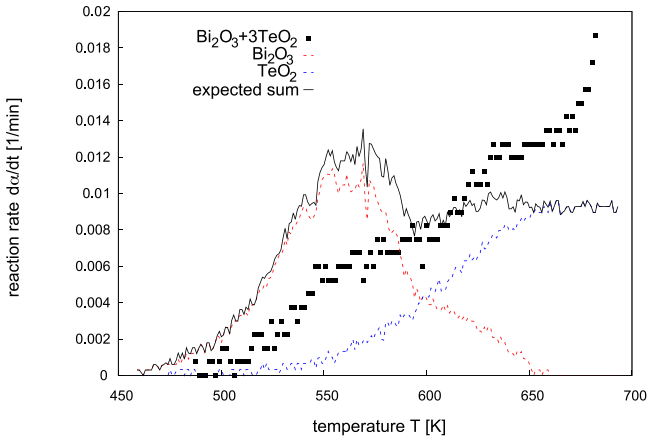

Fig. 13. Comparison of the reduction rate of mixed oxides compared with that of single bismuth and tellurium oxides normalized to their content in the mixture. Additionally, expected sum curve shows an algebraic sum of Bi_2O_3 and TeO_2 curves.

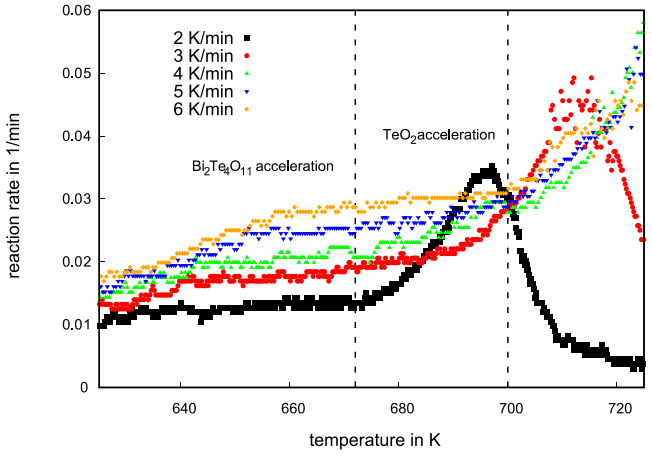

Fig. 14. Dependence of the reaction rate on the temperature in the region of initiation of faster part of the mixed oxides reduction.

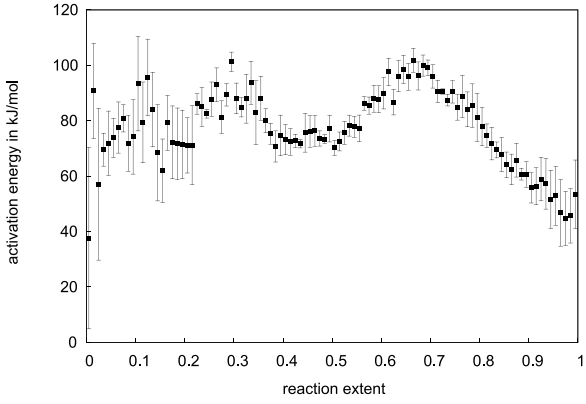

Fig. 15. Activation energy of mixed oxides reduction calculated with the Friedman method.

with isoconversional analysis are, within uncertainty range, close to 57 kJ/mol. The appropriate plots can be found in Supplementary Information (Figs. S20 and S21).

Additionally, the reduction of a mixture of the double oxides ($Bi_2Te_2O_7$ and $Bi_2Te_4O_{11}$) with 2:3 Bi:Te molar ratio was investigated. In order to provide good dispersion of the mixture constituents, the oxide material was obtained from a melt. The double oxide mixture was reduced similarly to its components. For each heating rate, two maxima are found in the reaction rate dependence. The temperatures, in which they occur, are similar to those of $Bi_2Te_2O_7$ and $Bi_2Te_4O_{11}$ reduction (see the comparison in Supplementary Information, Figs. S27-S31).

3.3. Reduction of mixed Bi_2O_3 and TeO_2

3.3.1. Structural transformations during the reaction

The structure of the powder during the reaction was investigated by interrupting the process, performed with a 3 K/min heating rate, at particular moments. SEM images of the partially reduced powders are presented in Fig. 9. It can be noticed, that up to 80% of the reaction extent, the grains have not grown significantly. At the end of the process, the grains' sizes change from hundreds of nanometres to few micrometres and platelets typical for Bi_2Te_3 are visible. It can be concluded, that the presence of different phases, in this case oxides, prevents bismuth telluride grains from growing.

XRD measurements were performed on partially reduced samples. The results of the XRD measurements of samples with 10%, 35%, and 80% of conversion are provided in Supplementary Information, Figs. S24-S26 together with the reference data. In the case of 10% of the reaction, starting oxides can be identified. Interestingly, a BiO_2 phase, with a higher bismuth oxidation state, was also found. In the material after 35% of reduction, bismuth telluride was detected together with bismuth oxide and tellurium oxide. After 80% of the process, which was reached in the last, faster part of the process, bismuth and tellurium double oxides, $Bi_2Te_2O_7$ and $Bi_2Te_4O_{11}$, were identified in the material. The $Bi_2Te_4O_{11}$ phase was found in its stable monoclinic structure [34].

Elemental analysis was performed on the material obtained during a reduction with a 4 K/min heating rate. Fig. 10 shows a cross-section of bismuth telluride grains embedded in an epoxy resin and maps of the concentration of elements obtained with the EDX method. The maps show a uniform distribution of the elements in the grains. The atomic ratio Bi:Te, calculated for the areas, where these elements were found, is equal to 0.608 ± 0.033. The value is close to the 0.667 expected for stoichiometric Bi_2Te_3. An almost total lack of oxide confirms that the material has been successfully reduced.

The same material was investigated with XPS spectroscopy. Prior to the measurement, the surface of the material was etched with Ar ions in order to remove any adsorbed species and the grains' surface oxidised in the air. No maxima corresponding to oxygen were found in the survey spectrum. The high resolution spectra for Bi4f and Te3d regions are presented in Fig. 11. Two peaks at 157.2 eV and 162.6 eV, corresponding to $Bi4f_{7/2}$ and $Bi4f_{5/2}$, are visible in the Bi4f region. A doublet with peaks at 572.0 eV and 582.3 eV is attributed to $Te3d_{5/2}$ and $Te3d_{3/2}$ photoelectrons. Both bismuth and tellurium spectra can be deconvoluted into a single doublet. It indicates that both elements were found in one valence state. The peaks' position values are characteristic for those measured for bismuth telluride earlier [37–40]. The results of the EDX and XPS measurements prove, that the reduction was completed.

3.3.2. Kinetic analysis

The reaction rate of the reduction of the mixed oxides is plotted *versus* the reaction extent in Fig. 12. Again, an increase in the reaction rate is visible in the final stage.

In order to determine the mutual influence of the oxides on their reduction behaviour before the increase of the reaction rate, data obtained for the same heating rate (2 K/min) for different materials were plotted in Fig. 13. Similar dependencies were found for experiments with other heating rates. The reaction rate for tellurium oxide was corrected by a factor of 2/3 (which is related to the amount of oxide bound with Te in the oxide mixture). The data for bismuth oxide was corrected by the factor of 1/3. A sum of the two latter reactions is presented with a black line. It shows different behaviour than the actually measured process, proving a mutual influence of the reactants on the reduction. It can be noticed, that the reduction of mixed oxides is

slower than that of bismuth oxide only. This may be a result of the decreased surface area available for the reaction.

The temperature region in which the reaction starts to accelerate is presented in Fig. 14. The exact temperature for measurements with 4, 5 and 6 K/min heating rates is similar to that observed for the reduction of TeO_2. In the case of the 2 K/min measurement, the temperature, in which the faster step begins, is nearly the same as for $Bi_2Te_4O_{11}$ reduction, and for 3 K/min is in between. Therefore, it can be concluded, that for low heating rates, the longer duration of the process allows for the formation of the double oxides. Consequently, in this case, the mechanisms of the reduction process should be similar to those of the reactions of double oxides. This is in agreement with the XRD results, revealing the presence of the double oxides during the reduction process. In the case of high heating rates, the reduction starts faster in terms of time and lasts a shorter time, which prevents double oxide synthesis.

Unexpectedly, the non-parametric analysis returned constant activation energy of the reduction of the mixed oxides across the whole temperature range, equal to (91.1 ± 0.2) kJ/mol. The exothermal effect is not as strong as for TeO_2 or $Bi_2Te_4O_{11}$ due to the higher bismuth concentration (in the form of Bi_2O_3 or $Bi_2Te_2O_7$). Therefore, the plot of the *h(T)* function in Arrhenius coordinates remains linear (see Fig. S32 in the Supplementary information). However, the activation energy is higher than for all other investigated materials. Moreover, the evaluated function *f* (black curve in Fig. 5) also differs from those obtained for the constituents of the reaction mixture.

In this case, the results of the isoconversional analysis, presented in Fig. 15, are more reliable. For up to 70% of the conversion, the values are similar to those obtained for single bismuth and tellurium oxides, 70–80 kJ/mol. After that, the activation energy decreases, reaching about 50 kJ/mol, which is close to the value found for double oxides reduction.

4. Conclusions

The kinetics of the hydrogen reduction of mixed Bi_2O_3 and TeO_2 oxides, leading to the formation of thermoelectric material Bi_2Te_3, was investigated. For a better understanding of the results, a similar analysis was also performed with bismuth and tellurium oxide, $Bi_2Te_2O_7$ and $Bi_2Te_4O_{11}$ double oxides.

The reduction of TeO_2 in the investigated temperature range has two steps. The first one can be described by the first-order reaction equation with activation energy equal to 69 kJ/mol. The second step starts at a temperature of about 700 K and is much faster than the first. Nanoparticles of the formed tellurium melt at this temperature, enhancing the reaction. Moreover, the heat released during the fast reduction locally increases the temperature, also speeding up the process.

The reduction of $Bi_2Te_2O_7$ has an autocatalytic behaviour, indicated by the high activation energy, over 150 kJ/mol, at the beginning of the process, which then decreases to 56 kJ/mol. A change of the reaction mechanism was also noticed in the results of the kinetic analysis. The dependence of the reaction rate on conversion is similar to the model derived for nucleation and growth controlled reactions.

The $Bi_2Te_4O_{11}$ reduction is separated into two steps, determined on the basis of the existence of two maxima in the reaction rate over the reaction extent plot. The first reaction rate maximum seems to be related to the reduction of the $Bi_2Te_2O_7$ substructure. The second maximum, as with TeO_2 reduction, causes a strong exothermal effect. However, its onset temperature is lower than for the tellurium oxide reaction.

Finally, the reduction of mixed bismuth and tellurium oxides was analysed. In the beginning, the reaction was slower, than it could be expected on the basis of the Bi_2O_3 reduction. This was assigned to the smaller surface area available for the hydrogen. More significant differences between single and mixed oxides reactions were found in the second, faster part of the process. It was noticed, that for low heating rates double oxides are formed. Thus, the reaction accelerates at the temperature corresponding to $Bi_2Te_4O_{11}$ reduction acceleration. In the case of high heating rates, there is no time enough for the synthesis of this phase. Therefore, the initiation of the second step occurs in the temperature characteristic for TeO_2. SEM imaging of partially reduced material showed, that there is no significant growth of grains until the end of the process.

Investigation of the reduction process in a multi-component oxide system shows, that a good understanding requires considering many factors – the initial state of the substrates (*e.g.* the grain size), phase transformations (melting and evaporation), catalytic effects and released heat. The evaluation of the reaction mechanisms is helpful in adjusting the parameters of the process.

Declaration of Competing Interest

None.

Acknowledgement

This work was supported by National Science Centre Poland [grant number 2016/21/B/ST8/03193].

Appendix A. Supplementary data

Supplementary material related to this article can be found, in the online version, at doi:https://doi.org/10.1016/j.tca.2019.178437.

References

[1] L. Teng, S. Noguchi, S. Seetharaman, Reduction kinetics of FeO-CoO solid solution by hydrogen gas, Metall. Mater. Trans. B Process Metall. Mater. Process. Sci. 38 (2007) 55–61, https://doi.org/10.1007/s11663-006-9006-1.
[2] M. Bahgat, M.-K. Paek, C.-H. Park, J.-J. Pak, Thermal synthesis of nanocrystalline (CoxNi1-x)yFe1-y KOVAR alloy through gaseous reduction of mixed oxides, Mater. Trans. 49 (2008) 208–214, https://doi.org/10.2320/matertrans.MER2007229.
[3] J.-J. Pak, M. Bahgat, B.-H. Kim, M.-K. Paek, Low temperature isothermal reduction kinetics of Fe_2O_3/NiO mixed oxides and comparative synthesis of Fe1-xNix alloys, Mater. Trans. 49 (2008) 352–359, https://doi.org/10.2320/matertrans.MRA2007203.
[4] B. Li, Y. Wei, H. Wang, Non-isothermal reduction kinetics of Fe_2O_3–NiO composites for formation of Fe–Ni alloy using carbon monoxide, Trans. Nonferrous Met. Soc. China 24 (2014) 3710–3715, https://doi.org/10.1016/S1003-6326(14)63519-6.
[5] D. Jelić, S. Zeljković, B. Škundrić, S. Mentus, Thermogravimetric study of the reduction of CuO–WO_3 oxide mixtures in the entire range of molar ratios, J. Therm. Anal. Calorim. 132 (2018) 77–90, https://doi.org/10.1007/s10973-017-6921-0.
[6] D. Vie, N. Valero, E. Martínez, F. Sapiña, J.-V. Folgado, A. Beltrán, A new approach to the synthesis of intermetallic compounds: mild synthesis of submicrometric CoxMy (M = Mo, W; x:y = 3:1 and 7:6) particles by direct reduction of freeze-dried precursors, J. Mater. Chem. 12 (2002) 1017–1021, https://doi.org/10.1039/b110798d.
[7] S. Gavriliu, M. Lungu, M. Lucaci, E. Enescu, New WAg electrical contacts with ultrafine structure for low voltage devices, J. Optoelectron. Adv. Mater. 8 (2006) 702–707.
[8] J.C. Juarez, R. Morales, Reduction kinetics of Ag_2MoO_4 by hydrogen, Metall. Mater. Trans. B 39 (2008) 738–745, https://doi.org/10.1007/s11663-008-9173-3.
[9] O.A. Bulavchenko, Z.S. Vinokurov, T.N. Afonasenko, P.G. Tsyrul'nikov, S.V. Tsybulya, A.A. Saraev, V.V. Kaichev, Reduction of mixed Mn–Zr oxides: in situ XPS and XRD studies, Dalton Trans. 44 (2015) 15499–15507, https://doi.org/10.1039/C5DT01440A.
[10] S.B. Sarkar, H.S. Ray, I. Chatterjee, Kinetics of reduction of iron ore—Coal pellets, J. Therm. Anal. 35 (1989) 2461–2469, https://doi.org/10.1007/BF01911910.
[11] K. Piotrowski, K. Mondal, H. Lorethova, L. Stonawski, T. Szymański, T. Wiltowski, Effect of gas composition on the kinetics of iron oxide reduction in a hydrogen production process, Int. J. Hydrogen Energy (2005), https://doi.org/10.1016/j.ijhydene.2004.10.013.
[12] A. Maleki, N. Hosseini, B. Niroumand, A review on aluminothermic reaction of Al/ZnO system, Ceram. Int. 44 (2018) 10–23, https://doi.org/10.1016/J.CERAMINT.2017.09.168.
[13] J.J. Ritter, A novel synthesis of polycrystalline bismuth telluride, Inorg. Chem. 33 (1994) 6419–6420, https://doi.org/10.1021/ic00104a065.
[14] J.J. Ritter, P. Maruthamuthu, Synthesis of fine-powder polycrystalline Bi – Se – Te, Bi – Sb – Te, and Bi – Sb – Se – Te alloys, Inorg. Chem. 36 (1997) 260–263, https://doi.org/10.1021/ic960616i.
[15] M. Saleemi, M.S. Toprak, S. Li, M. Johnsson, M. Muhammed, Synthesis, processing, and thermoelectric properties of bulk nanostructured bismuth telluride (Bi_2Te_3), J.

Mater. Chem. 22 (2012) 725–730, https://doi.org/10.1039/C1JM13880D.
[16] G. Lee, G. Ha, Synthesis of Bi0.5Sb1.5Te3 thermoelectric powder using an oxide-reduction process, J. Korean Inst. Electr. Electron. Mater. Eng. 43 (2014) 1697–1702, https://doi.org/10.1007/s11664-013-2846-y.
[17] Y.S. Lim, S.M. Wi, G.G. Lee, Synthesis of n-type Bi2Te1-xSex compounds through oxide reduction process and related thermoelectric properties, J. Eur. Ceram. Soc. 37 (2017) 3361–3366, https://doi.org/10.1016/j.jeurceramsoc.2017.04.020.
[18] B. Bochentyn, J. Karczewski, T. Miruszewski, B. Kusz, Structure and thermoelectric properties of Bi–Te alloys obtained by novel method of oxide substrates reduction, J. Alloys Compd. 646 (2015) 1124–1132, https://doi.org/10.1016/J.JALLCOM.2015.06.127.
[19] N. Gostkowska, T. Miruszewski, B. Trawiński, B. Bochentyn, B. Kusz, Structure and thermoelectric properties of Cs-Bi-Te alloys fabricated by different routes of reduction of oxide reagents, Solid State Sci. 73 (2017) 41–50, https://doi.org/10.1016/j.solidstatesciences.2017.07.016.
[20] B. Trawiński, B. Bochentyn, N. Gostkowska, M. Łapiński, T. Miruszewski, B. Kusz, Structure and thermoelectric properties of bismuth telluride—Carbon composites, Mater. Res. Bull. 99 (2018) 10–17, https://doi.org/10.1016/j.materresbull.2017.10.043.
[21] K.T. Kim, T.S. Lim, G.H. Ha, Improvement in thermoelectric properties of N-Type bismuth telluride nanopowders by hydrogen reduction treatment, Rev. Adv. Mater. Sci. 28 (2011) 196–199.
[22] S. Vyazovkin, A.K. Burnham, J.M. Criado, L.A. Pérez-Maqueda, C. Popescu, N. Sbirrazzuoli, ICTAC kinetics committee recommendations for performing kinetic computations on thermal analysis data, Thermochim. Acta 520 (2011) 1–19, https://doi.org/10.1016/j.tca.2011.03.034.
[23] G.B. Taylor, H.W. Starkweather, Reduction of metal oxides by hydrogen, J. Am. Chem. Soc. 52 (1930) 2314–2325, https://doi.org/10.1021/ja01369a019.
[24] B. Janković, B. Adnad, S. Mentus, The kinetic analysis of non-isothermal nickel oxide reduction in hydrogen atmosphere using the invariant kinetic parameters method, Thermochim. Acta 456 (2007) 48–55, https://doi.org/10.1016/j.tca.2007.01.033.
[25] J. Šesták, The quandary aspects of non-isothermal kinetics beyond the ICTAC kinetic committee recommendations, Thermochim. Acta 611 (2015) 26–35, https://doi.org/10.1016/J.TCA.2015.04.026.
[26] M. Maciejewski, Computational aspects of kinetic analysis. Part B: the ICTAC Kinetics Project – the decomposition kinetics of calcium carbonate revisited, or some tips on survival in the kinetic minefield, Thermochim. Acta 355 (2000) 145–154, https://doi.org/10.1016/S0040-6031(00)00444-5.
[27] K.V. Manukyan, A.G. Avetisyan, C.E. Shuck, H.A. Chatilyan, S. Rouvimov, S.L. Kharatyan, A.S. Mukasyan, Nickel oxide reduction by hydrogen: kinetics and structural transformations, J. Phys. Chem. C 119 (2015) 16131–16138, https://doi.org/10.1021/acs.jpcc.5b04313.
[28] V.B. Chernogorenko, K.A. Lynchak, Production of bismuth powder by the reduction of bismuth oxide with a mixture of molecular and atomic hydrogen, Sov. Powder Metall. Met. Ceram. 12 (1973) 360–362, https://doi.org/10.1007/BF00791258.
[29] F. Korkmaz, S. Cetinkaya, S. Eroglu, Thermodynamic analysis and reduction of bismuth oxide by ethanol, Metall. Mater. Trans. B 47 (2016) 2378–2385, https://doi.org/10.1007/s11663-016-0686-x.
[30] B. Trawiński, B. Bochentyn, B. Kusz, A study of a reduction of a micro- and nanometric bismuth oxide in hydrogen atmosphere, Thermochim. Acta 669 (2018) 99–108, https://doi.org/10.1016/J.TCA.2018.09.010.
[31] R. Serra, J. Sempere, R. Nomen, A new method for the kinetic study of thermoanalytical data: the non-parametric kinetics method, Thermochim. Acta 316 (1998) 37–45, https://doi.org/10.1016/S0040-6031(98)00295-0.
[32] G. Guisbiers, L.C. Mimun, R. Mendoza-Cruz, K.L. Nash, Synthesis of tunable tellurium nanoparticles, Semicond. Sci. Technol. 32 (2017) 04LT01, , https://doi.org/10.1088/1361-6641/aa6173.
[33] X. Su, F. Fu, Y. Yan, G. Zheng, T. Liang, Q. Zhang, X. Cheng, D. Yang, H. Chi, X. Tang, Q. Zhang, C. Uher, Self-propagating high-temperature synthesis for compound thermoelectrics and new criterion for combustion processing, Nat. Commun. 5 (2014) 4908, https://doi.org/10.1038/ncomms5908.
[34] Z. Szaller, L. Pöppl, G. Lovas, I. Dódony, Study of the formation of Bi2Te4O11, J. Solid State Chem. 121 (1996) 251–261, https://doi.org/10.1006/JSSC.1996.0036.
[35] G.A. Lovas, I. Dódony, L. Pöppl, Z. Szaller, On the phase transitions of Bi_2Te_4O11, J. Solid State Chem. 135 (1998) 175–181, https://doi.org/10.1006/JSSC.1997.7594.
[36] O. Masson, P. Thomas, O. Durand, T. Hansen, J. Champarnaud, D. Mercurio, On the structure of the disordered Bi_2Te_4O11 phase, J. Solid State Chem. 177 (2004) 2168–2176, https://doi.org/10.1016/J.JSSC.2004.03.010.
[37] P. Kumar, P. Srivastava, J. Singh, R. Belwal, M.K. Pandey, K.S. Hui, K.N. Hui, K. Singh, Morphological evolution and structural characterization of bismuth telluride (Bi_2Te_3) nanostructures, J. Phys. D Appl. Phys. 46 (2013) 285301, , https://doi.org/10.1088/0022-3727/46/28/285301.
[38] D. Music, K. Chang, P. Schmidt, F.N. Braun, M. Heller, S. Hermsen, P.J. Pöllmann, T. Schulzendorff, C. Wagner, On atomic mechanisms governing the oxidation of Bi_2Te_3, J. Phys. Condens. Matter. 29 (2017) 485705, , https://doi.org/10.1088/1361-648X/aa945f.
[39] S. Liu, N. Peng, Y. Bai, D. Ma, F. Ma, K. Xu, Self-formation of thickness tunable Bi_2Te_3 nanoplates on thin films with enhanced thermoelectric performance, RSC Adv. 6 (2016) 31668–31674, https://doi.org/10.1039/C5RA26835D.
[40] J. Fu, S. Song, X. Zhang, F. Cao, L. Zhou, X. Li, H. Zhang, Bi_2Te_3 nanoplates and nanoflowers: synthesized by hydrothermal process and their enhanced thermoelectric properties, CrystEngComm 14 (2012) 2159, https://doi.org/10.1039/c2ce06348d.

Supplementary Information

A study of the kinetics of bismuth telluride synthesis by an oxide reduction method

Bartosz Trawiński, Beata Bochentyn, Marcin Łapiński, Bogusław Kusz

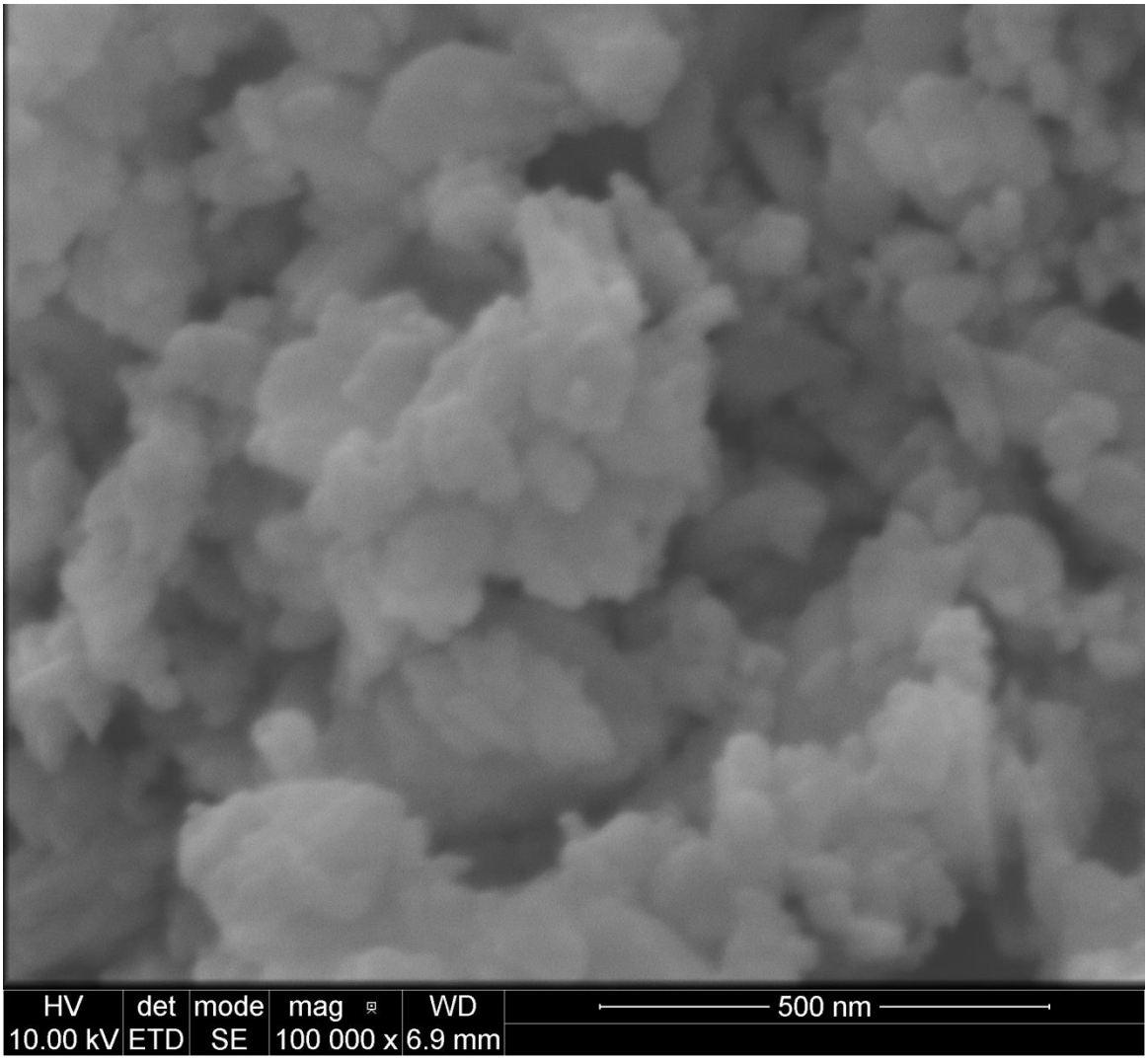

Fig. S1. SEM image of milled Bi_2O_3 powder

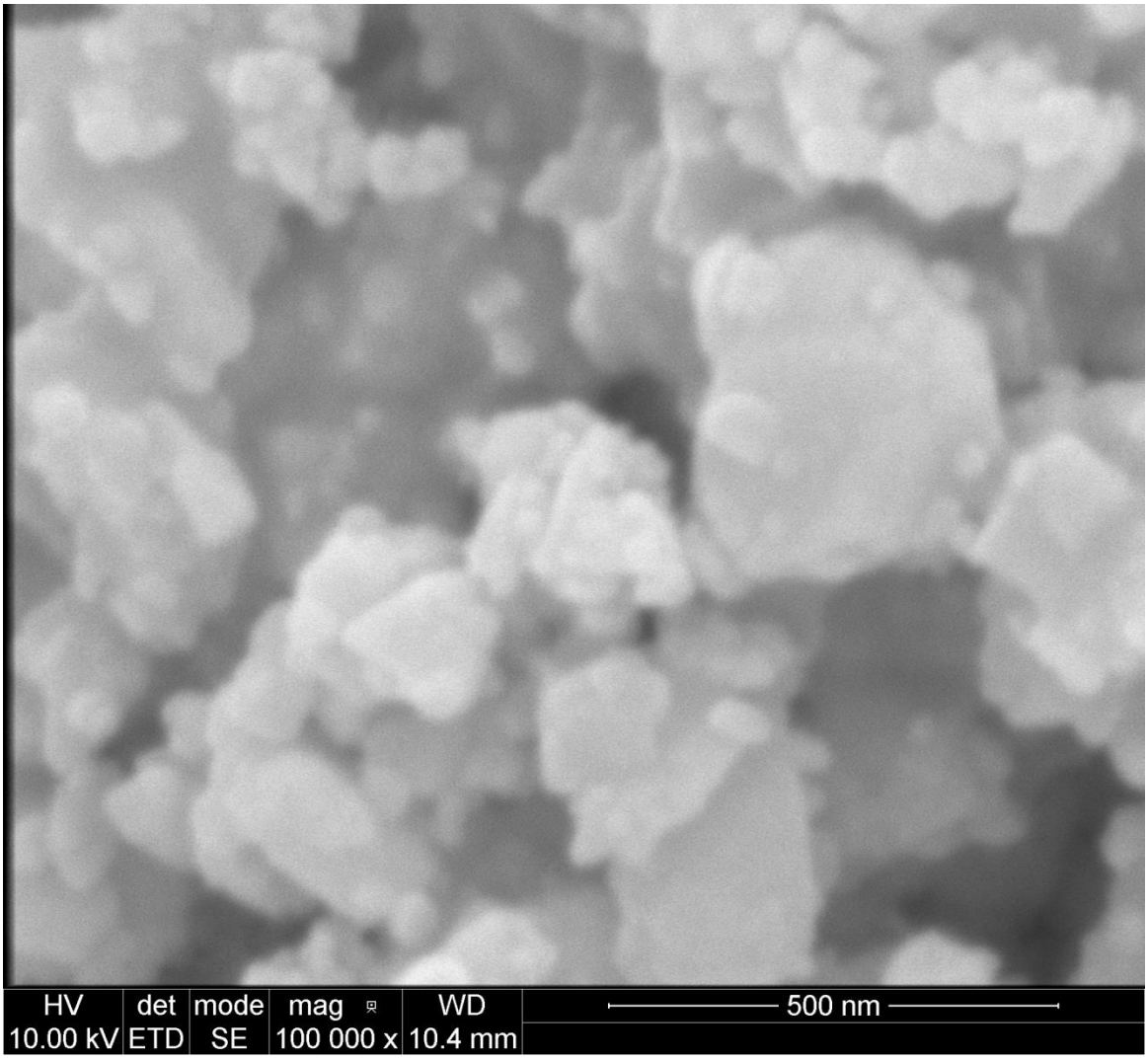

Fig. S2. SEM image of milled TeO_2 powder

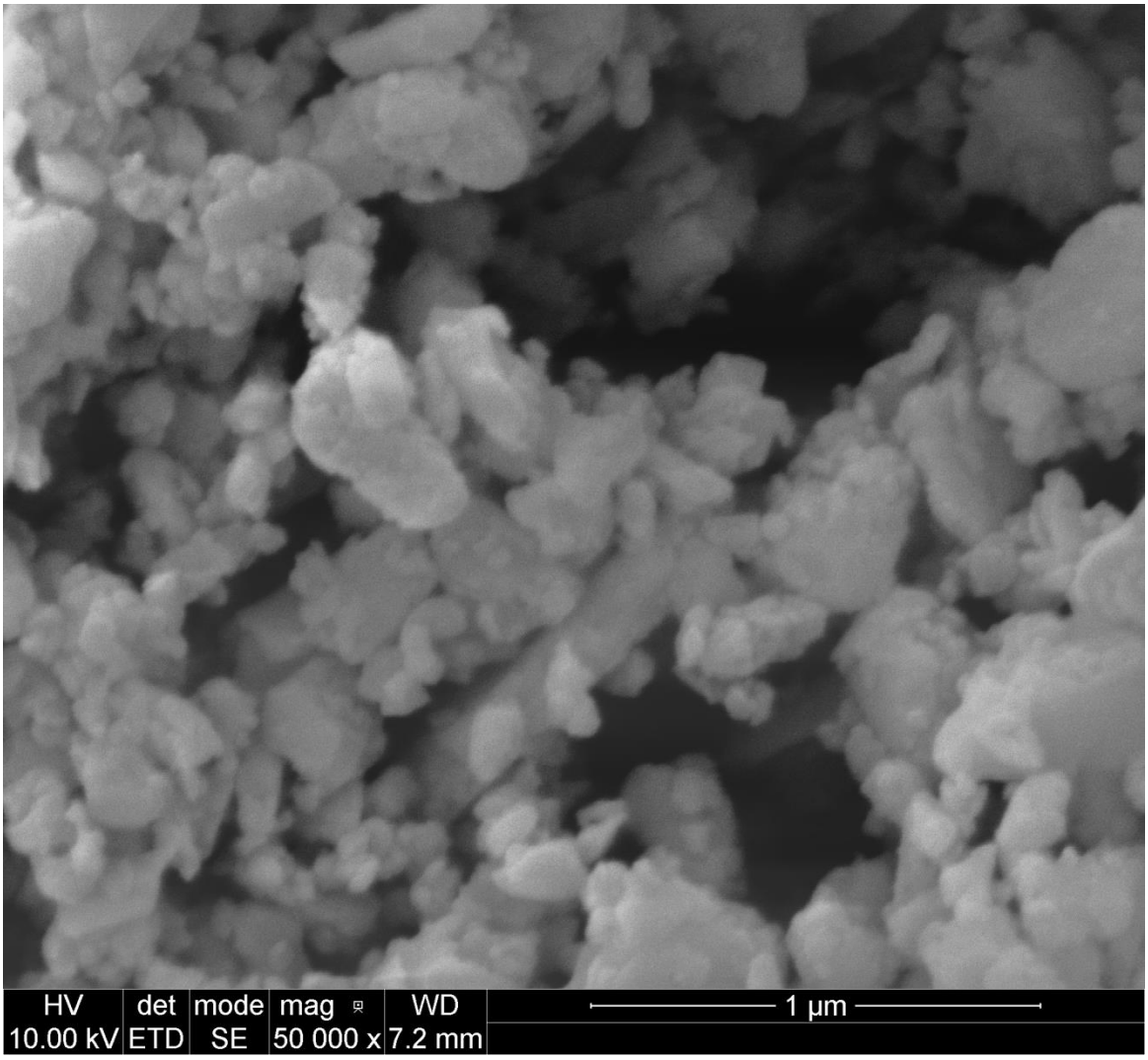

Fig. S3. SEM image of milled $Bi_2Te_7O_7$ powder

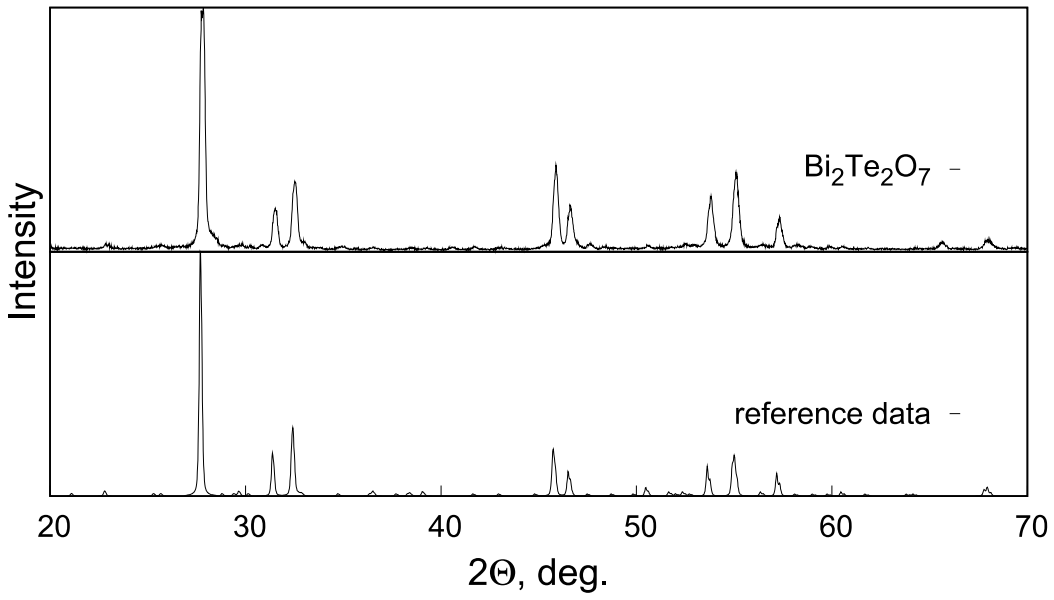

Fig. S4. XRD pattern of synthesized $Bi_2Te_2O_7$

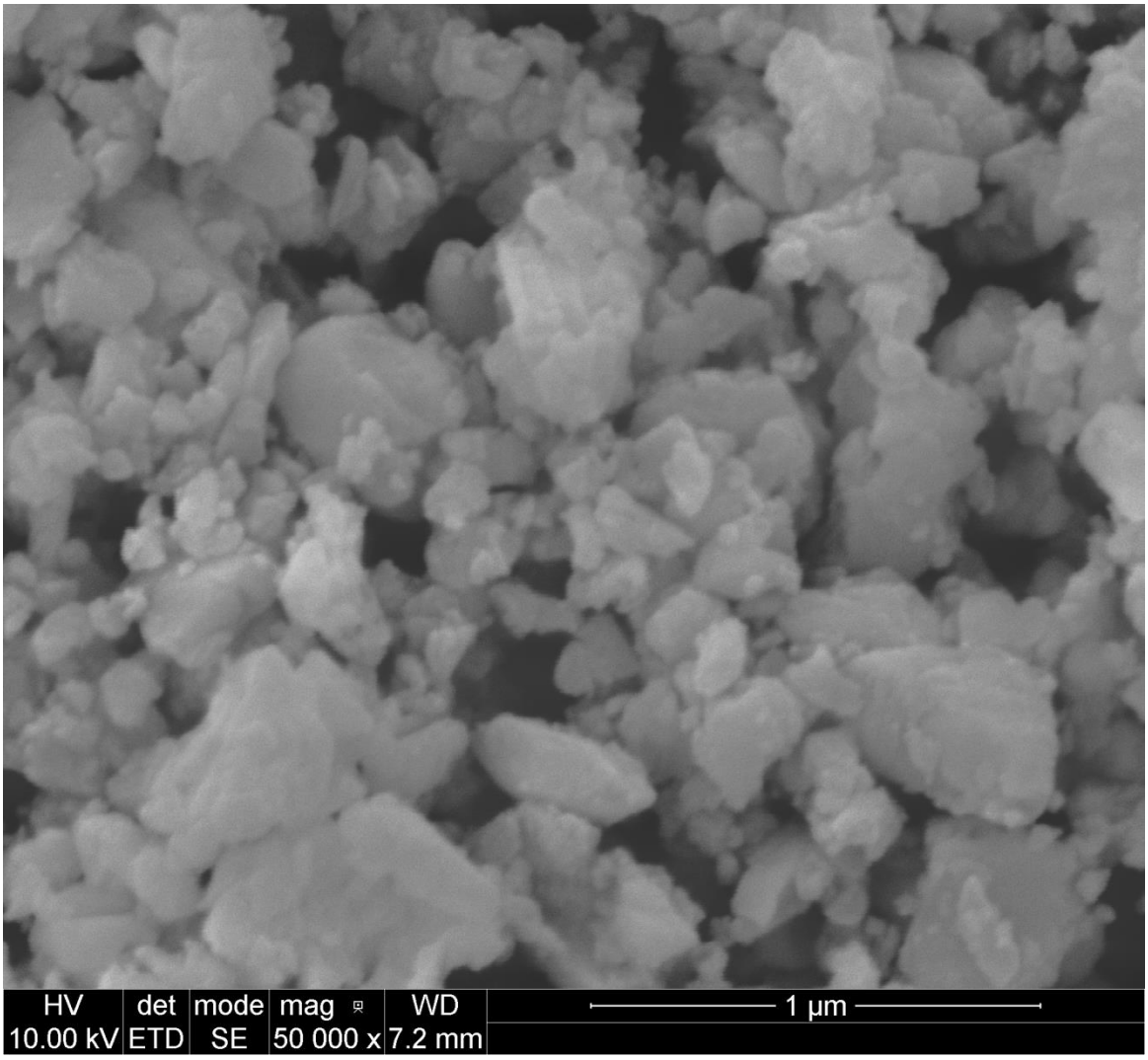

Fig. S5. SEM image of milled $Bi_2Te_4O_{11}$ powder

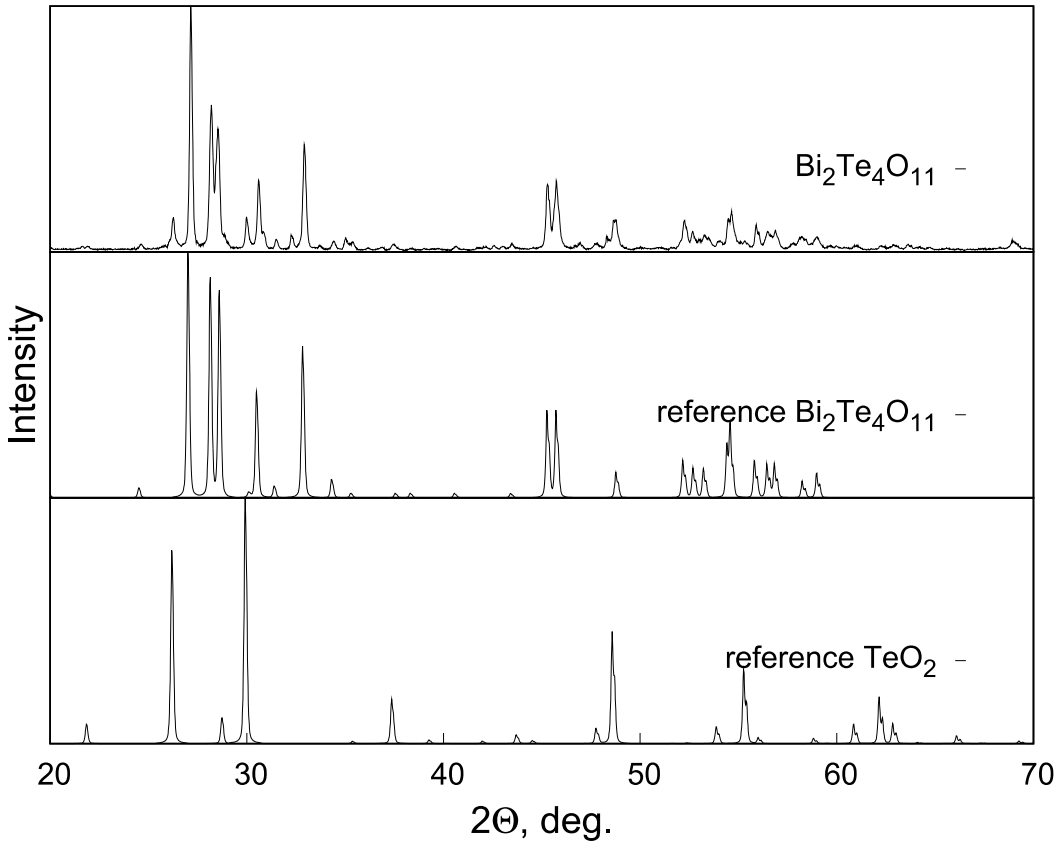

Fig. S6. XRD pattern of synthesized $Bi_2Te_4O_{11}$

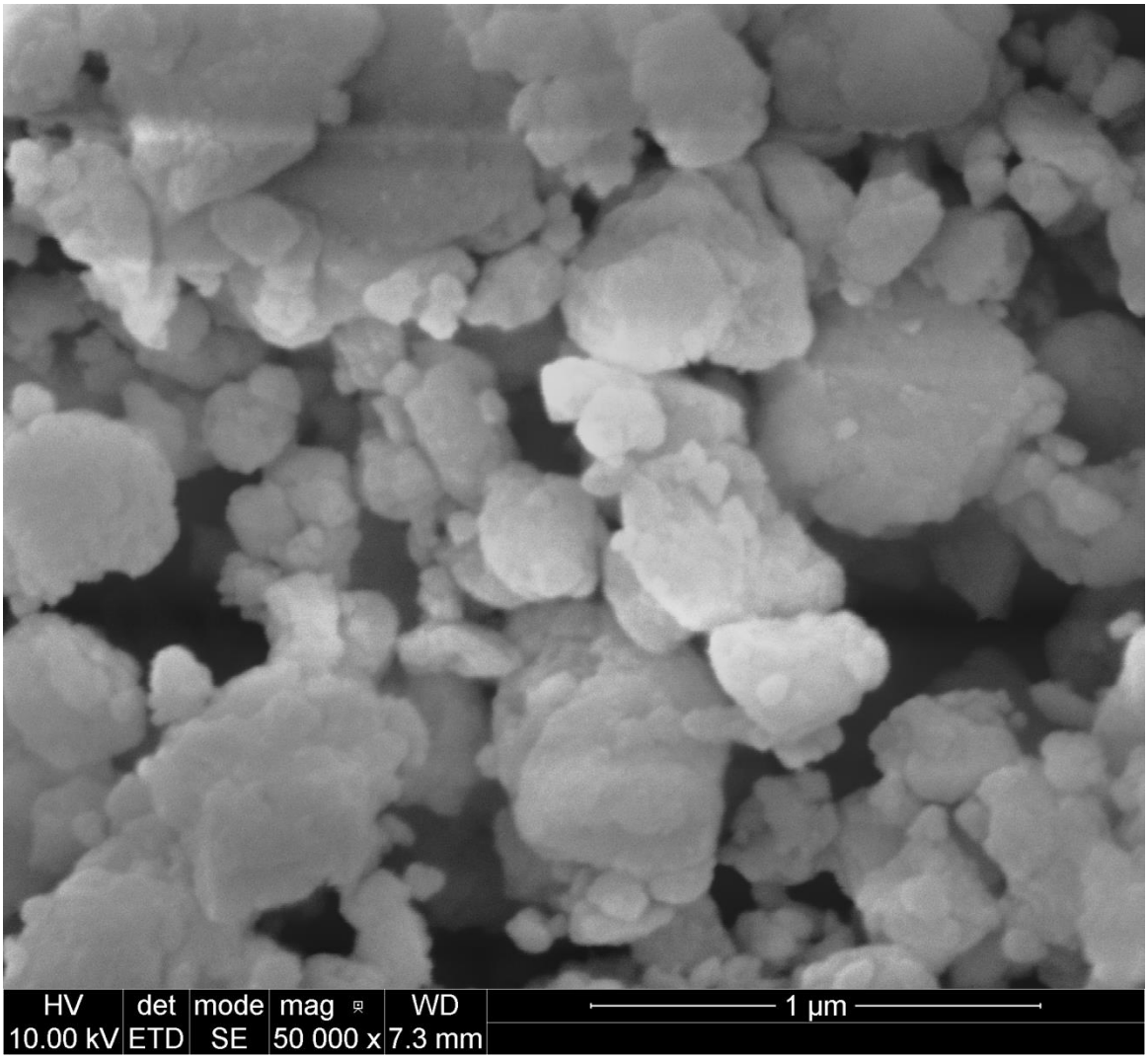

Fig. S7. SEM image of milled $Bi_2Te_3O_x$ ($Bi_2Te_2O_7$+$Bi_2Te_4O_{11}$) powder

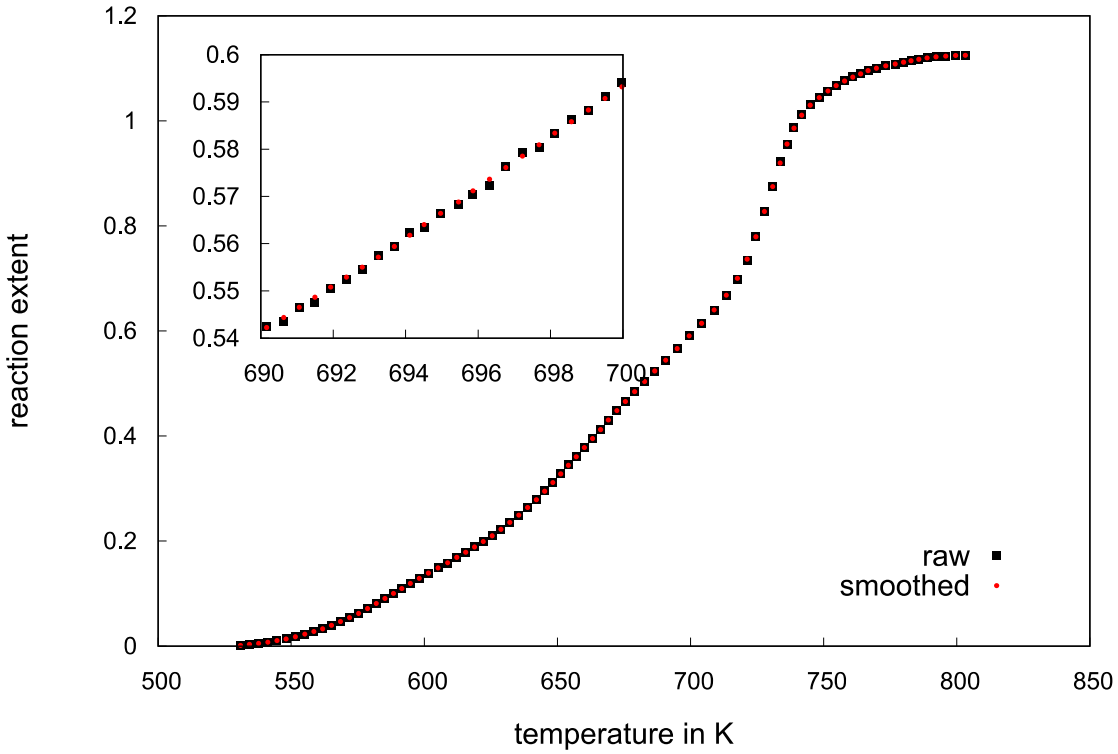

Fig. S8. Example of raw and smoothed measurement data - a result of Bi_2O_3+TeO_2 reduction with a 4 K/min heating rete. In the main graph every 10^{th} point is presented for clarity.

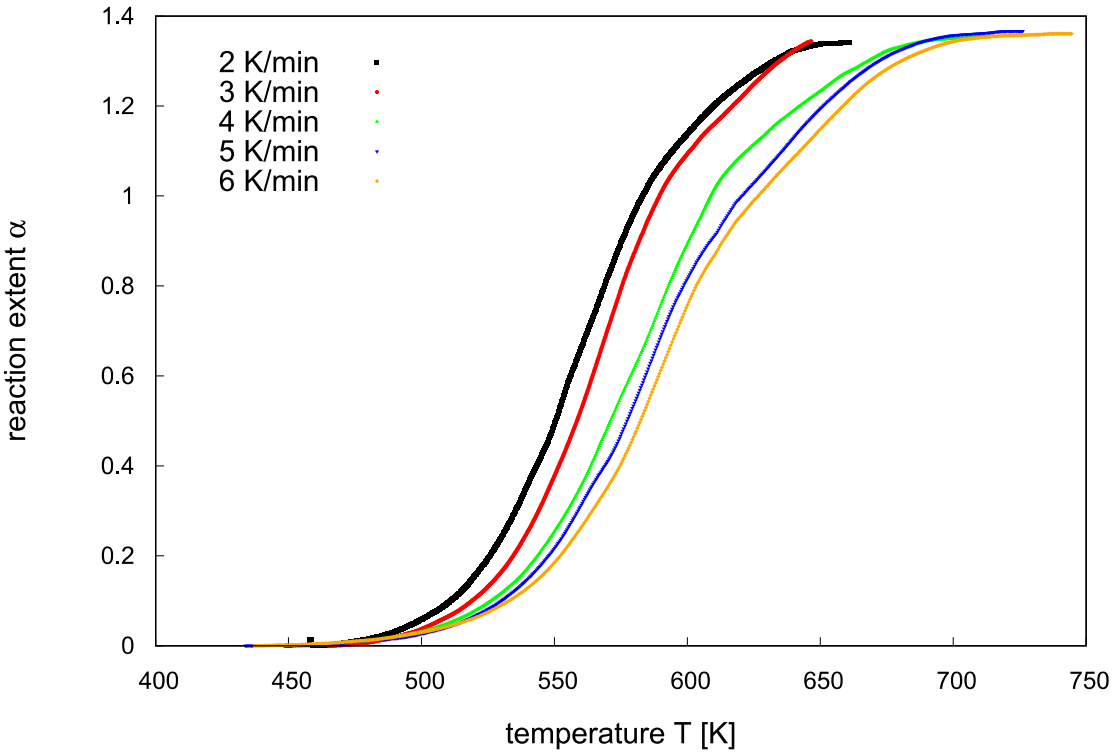

Fig. S9. Dependence of reaction extent on temperature for Bi_2O_3 reduction.

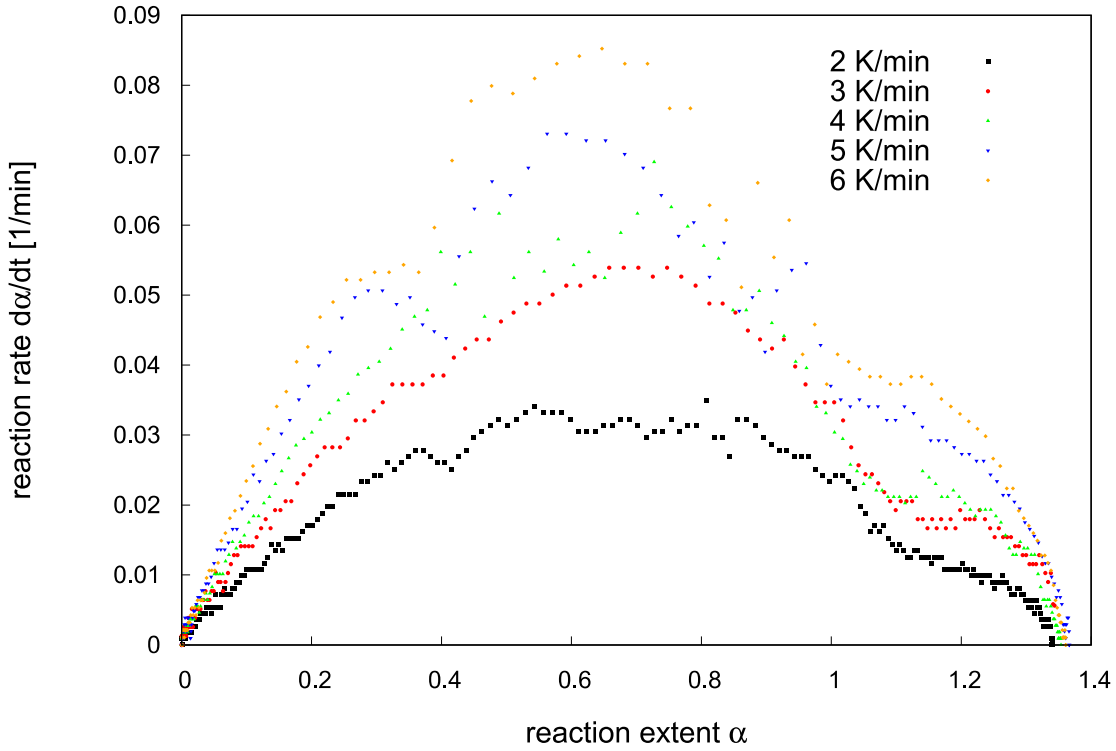

Fig. S10. Dependence of reaction rate on reaction extent for Bi_2O_3 reduction.

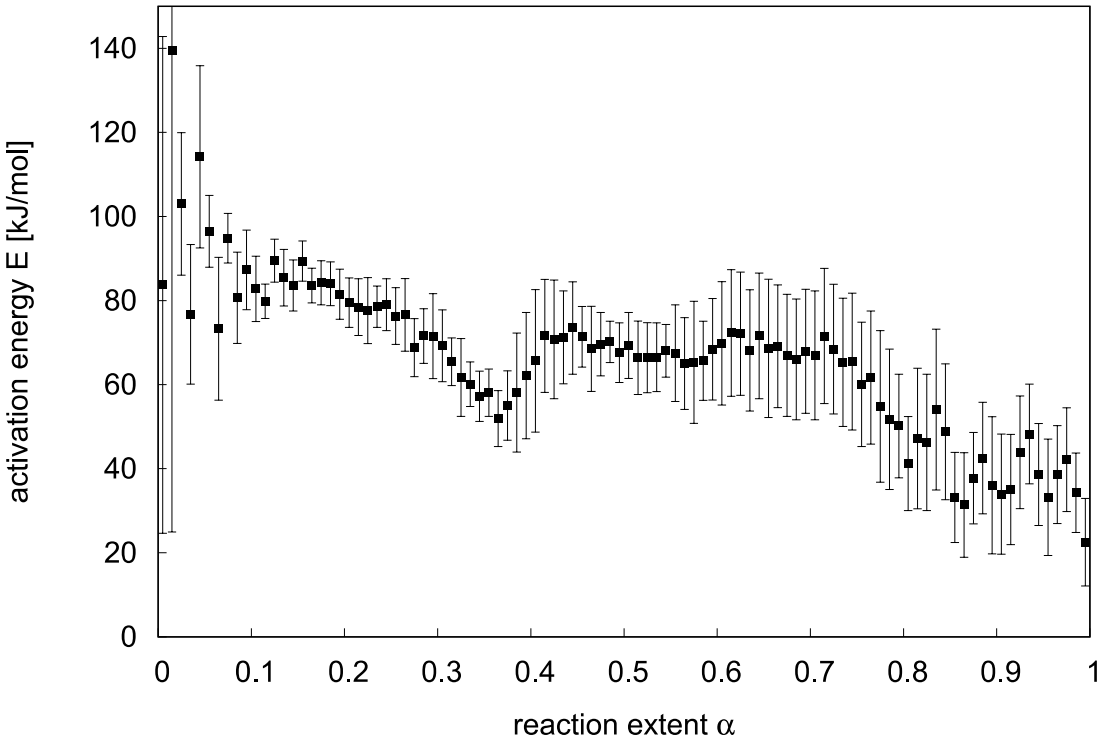

Fig. S11. Dependence of activation energy on the reaction extent during the Bi_2O_3 reduction obtained from isoconversional analysis

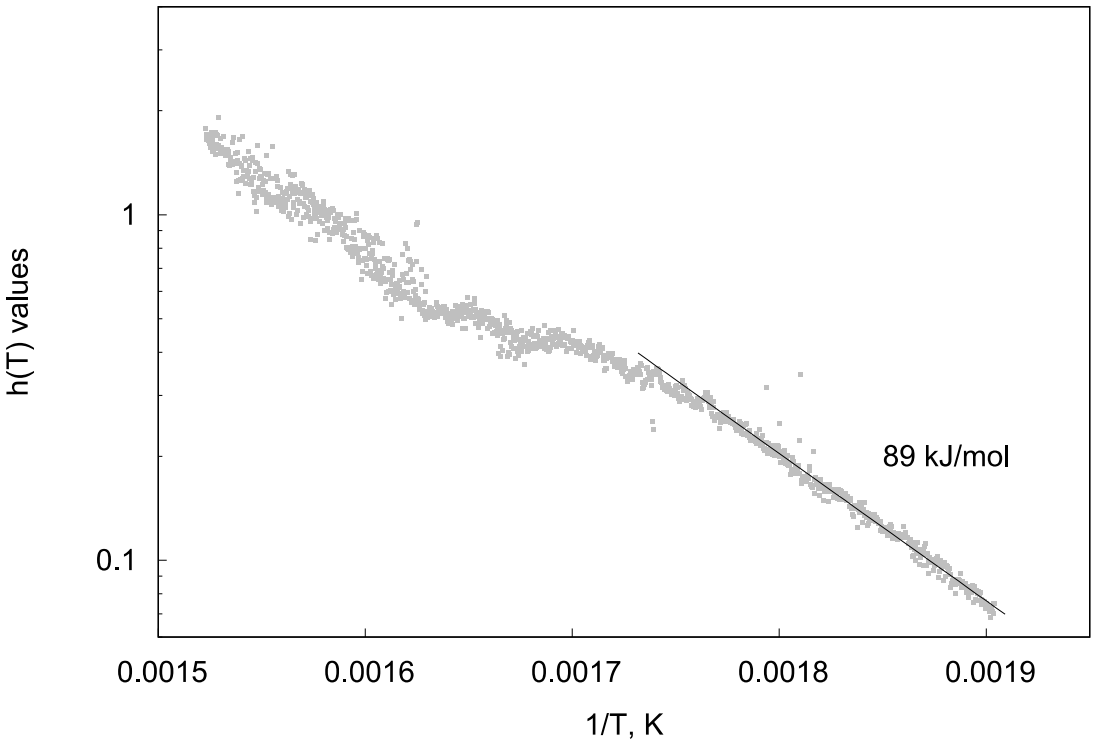

Fig. S12. Thermal function h(T) obtained from non-parametric analysis of the Bi_2O_3 reaction

Notice, that at the beginning of the process, the activation energy values obtained with both methods are consistent. At the end of the reactions results are different. However, the isoconversional analysis results can be considered more reliable in this case, because the reaction is strongly dependent on α.

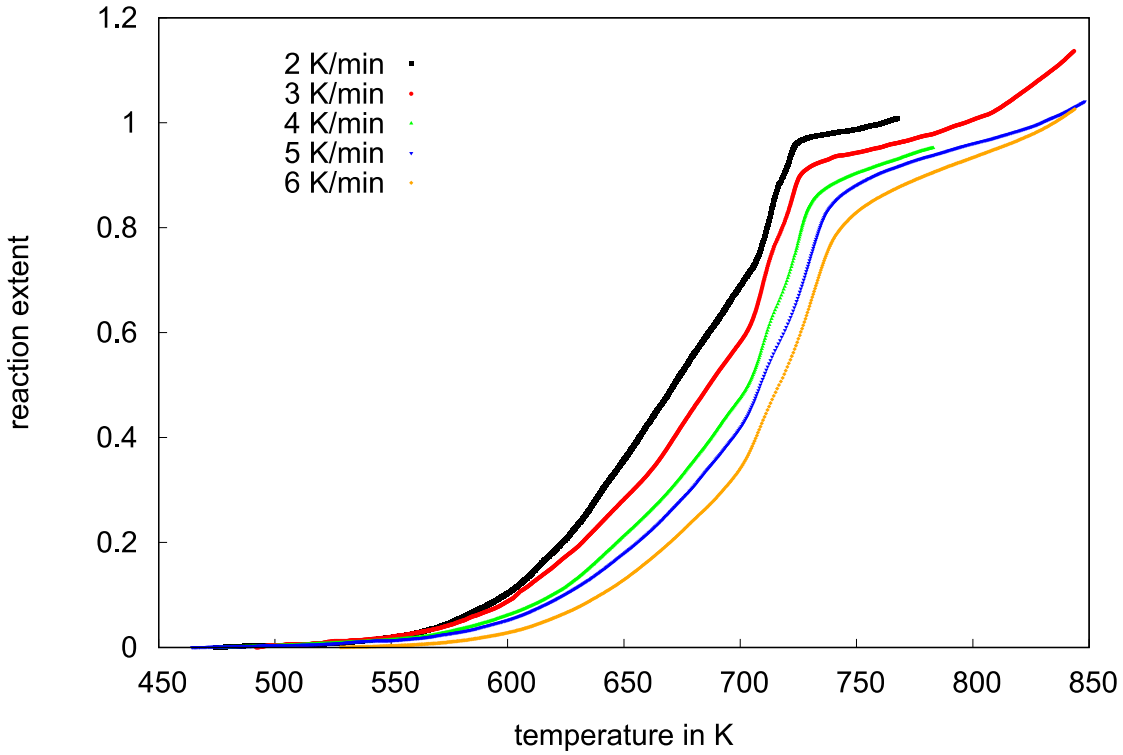

Fig. S13. Dependence of reaction extent on temperature for TeO_2 reduction

.

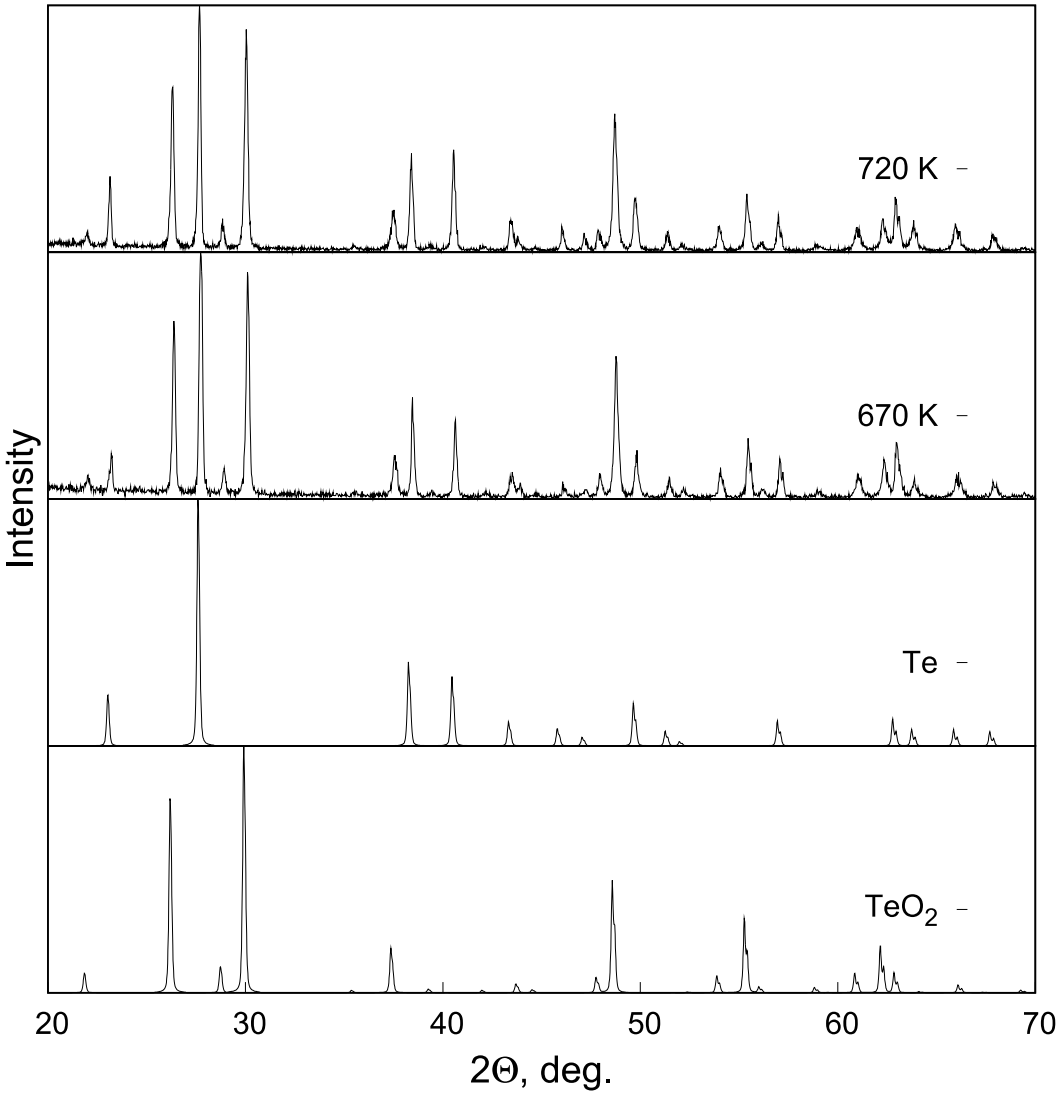

Fig. S14. XRD patterns of the tellurium oxide powder reduced up to 670 K (2 K/min heating rate) and 720 K (2 K/min) with reference patterns

Reference data from Powder Diffraction File:
TeO_2: 01-078-1713_10
Te: 00-0004-0554_11

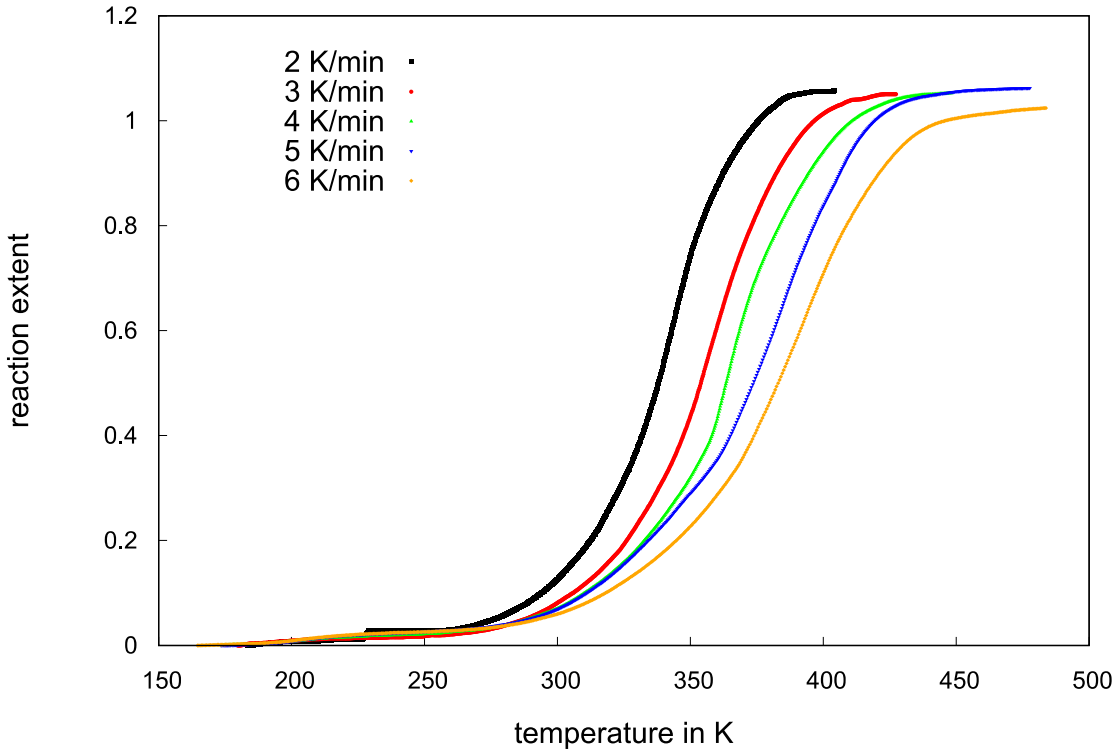

Fig. S15. Dependence of reaction extent on temperature for $Bi_2Te_2O_7$ reduction

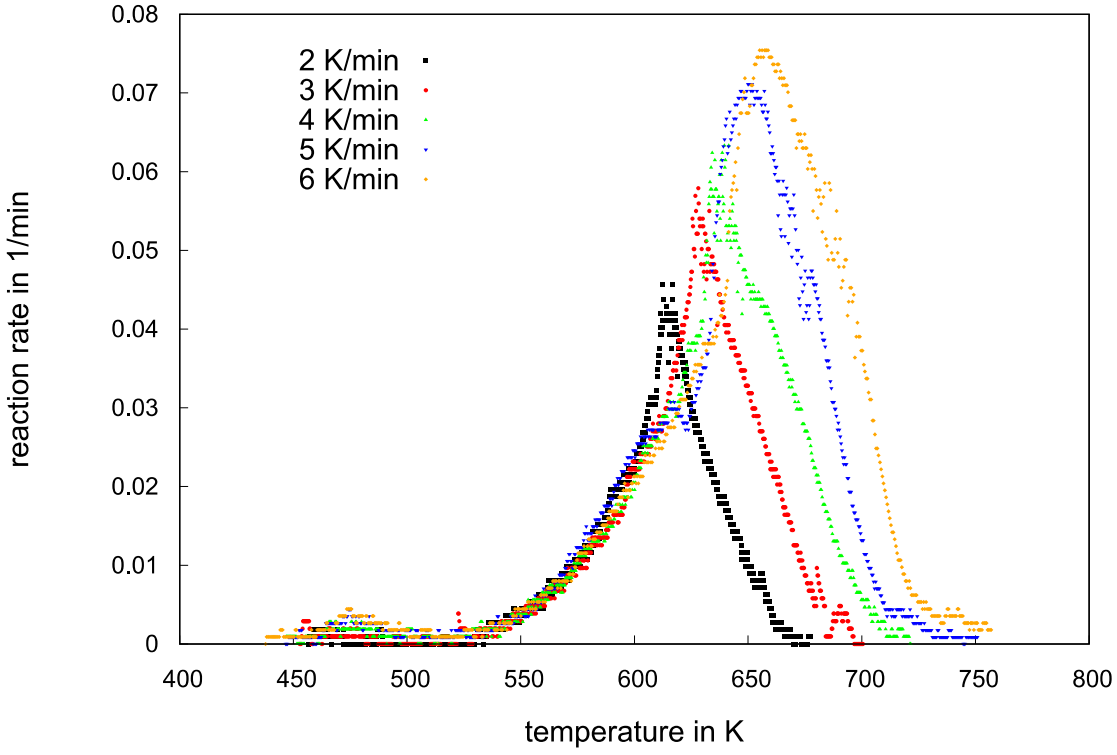

Fig S16. Dependence of the reaction rate on temperature during the $Bi_2Te_2O_7$ reduction with different heating rates

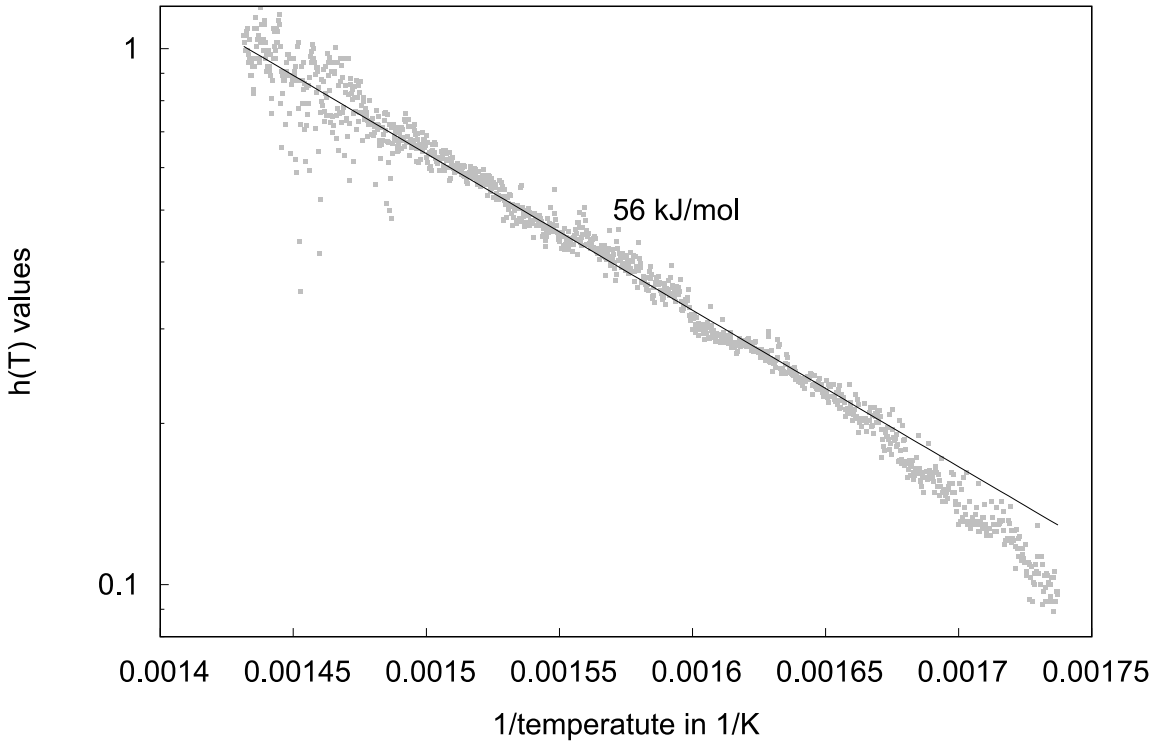

Fig. S17. Thermal function h(T) obtained from non-parametric analysis of the $Bi_2Te_2O_7$ reaction data

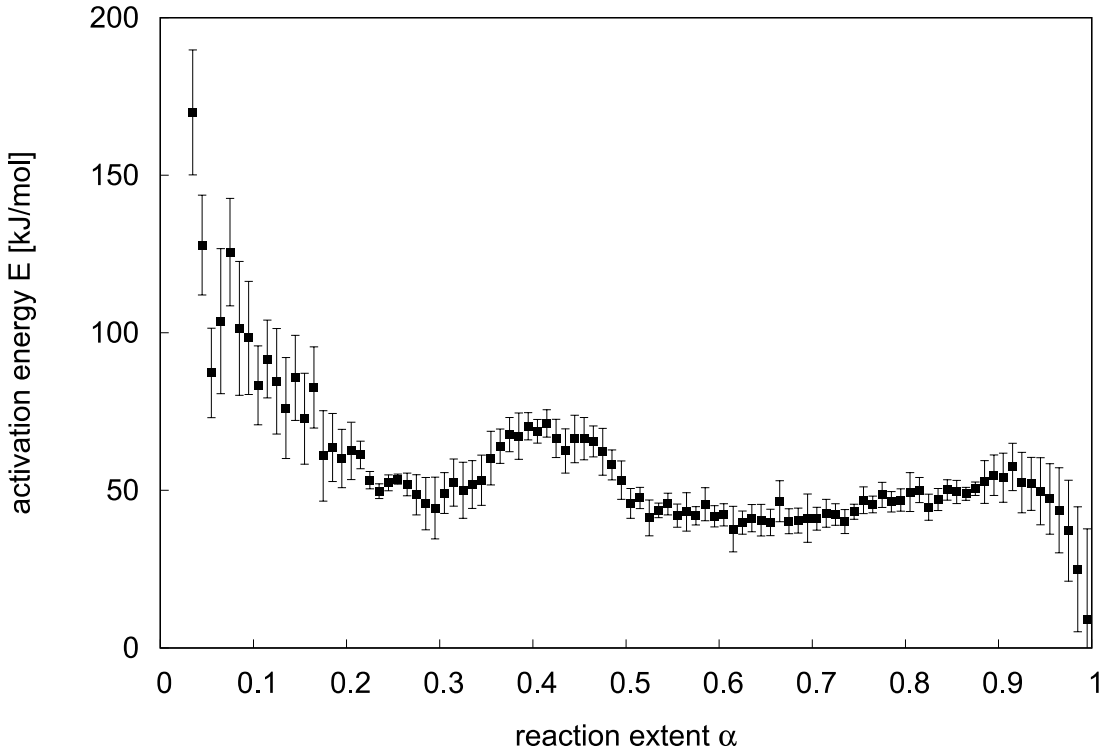

Fig. S18. Dependence of activation energy on the reaction extent during the $Bi_2Te_2O_7$ reduction obtained from isoconversional analysis.

The local maximum about 40% conversion is related with a shift of the maximum of the dependence of reaction rate on the conversion (Fig. 7). However, this maximum is not occurring or starting in similar temperature for different heating rates.

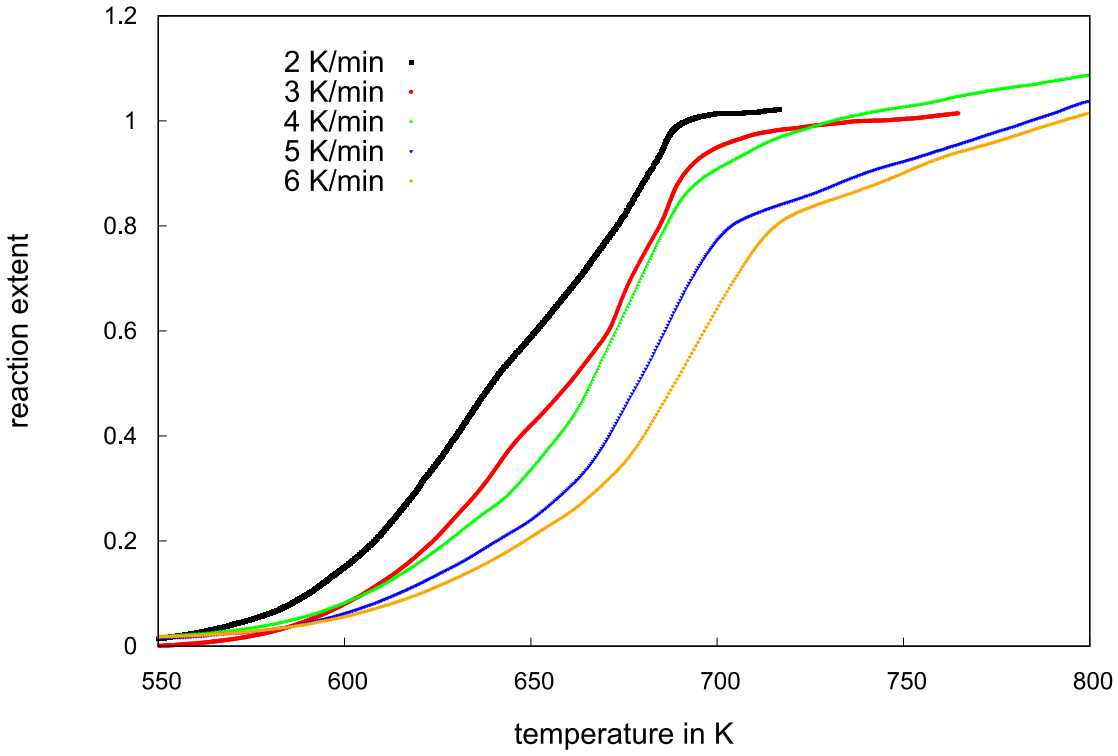

Fig. S19. Dependence of reaction extent on temperature for $Bi_2Te_4O_{11}$ reduction

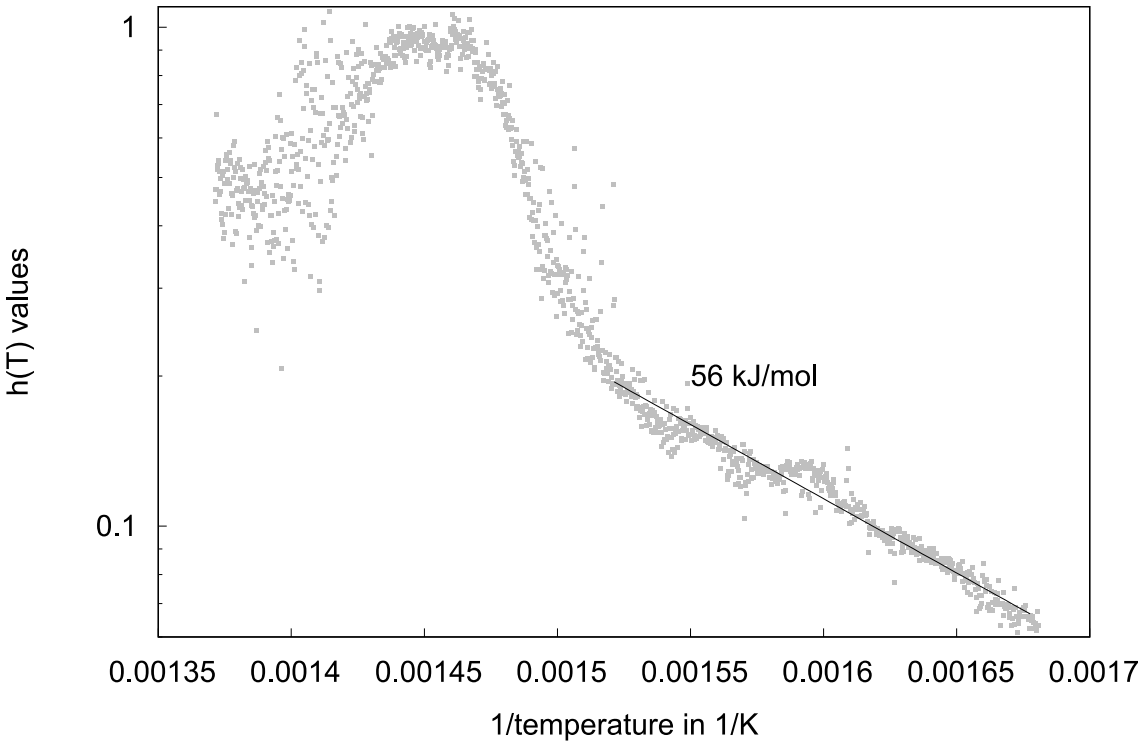

Fig. S20. Thermal function h(T) obtained from non-parametric analysis of the $Bi_2Te_4O_{11}$ reaction

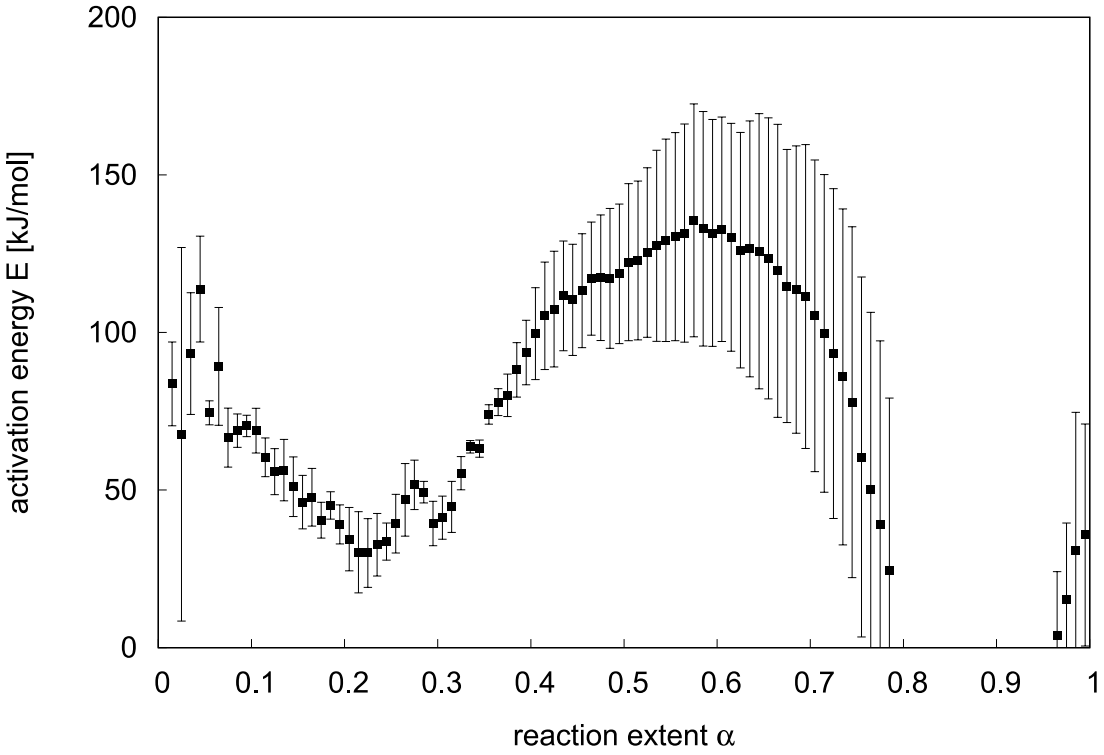

Fig. S21. Dependence of activation energy on the reaction extent during the $Bi_2Te_4O_{11}$ reduction obtained from isoconversional analysis

Like for the TeO2 reduction, the activation energy values for conversion higher than 30% are unreliable because the assumption of the isoconversional principle is not fulfilled.

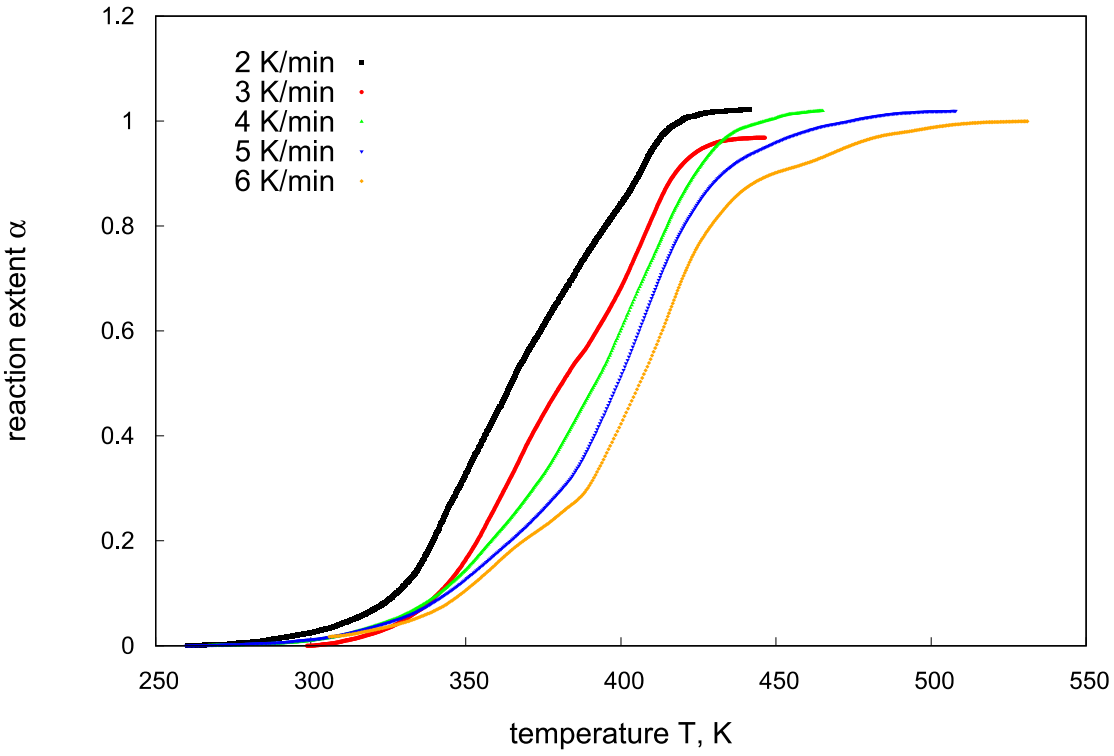

Fig. S22. Dependence of reaction extent on temperature for $Bi_2Te_2O_7$+$Bi_2Te_4O_{11}$ reduction

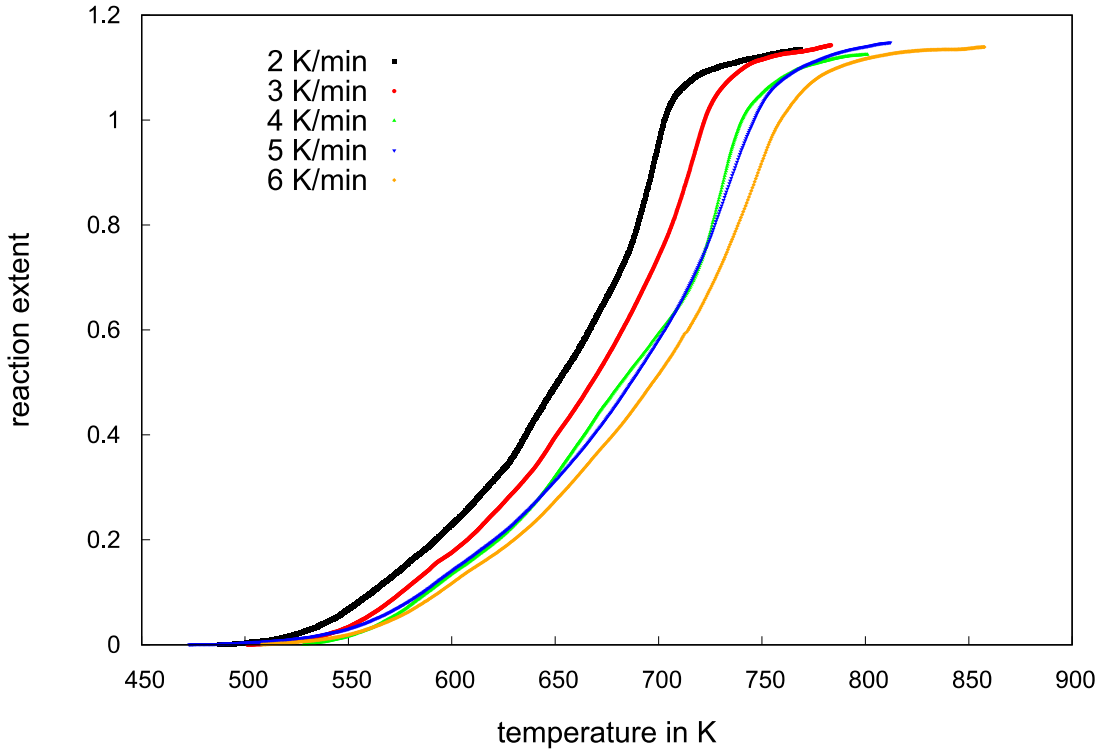

Fig. S23. Dependence of reaction extent on temperature for Bi_2O_3+TeO_2 reduction

XRD PATTERNS OF PARTIALLY REDUCED MIXED OXIDES, 3 K/MIN HEATING RATE

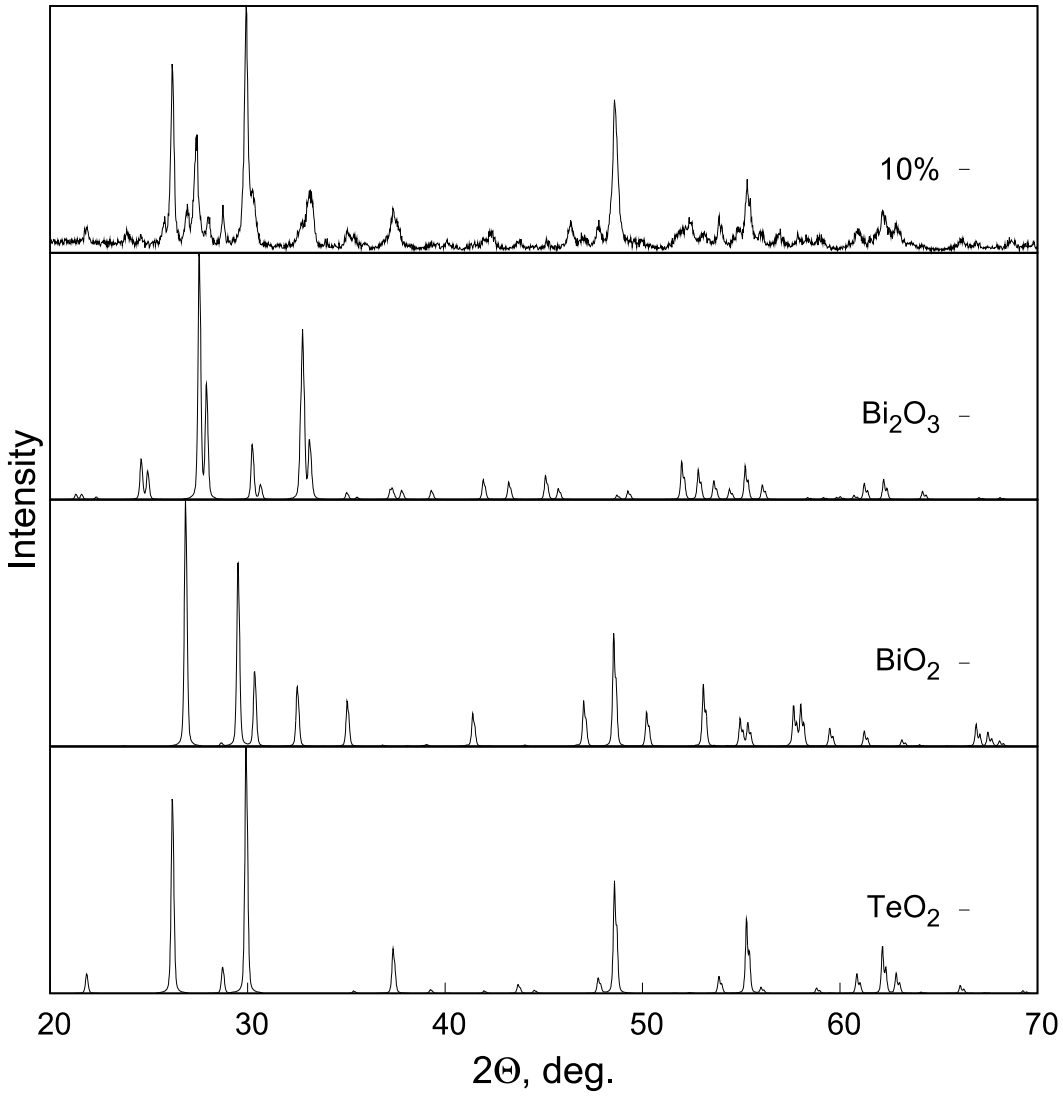

Fig. S24. XRD pattern of the material after 10% of the reaction

The 27.5° peak can be identified as BiO_2 reflection.

Reference data from Powder Diffraction File:
Bi_2O_3: 00-050-1088_11
BiO_2: 01-083-0410_14
TeO_2: 01-078-1713_10

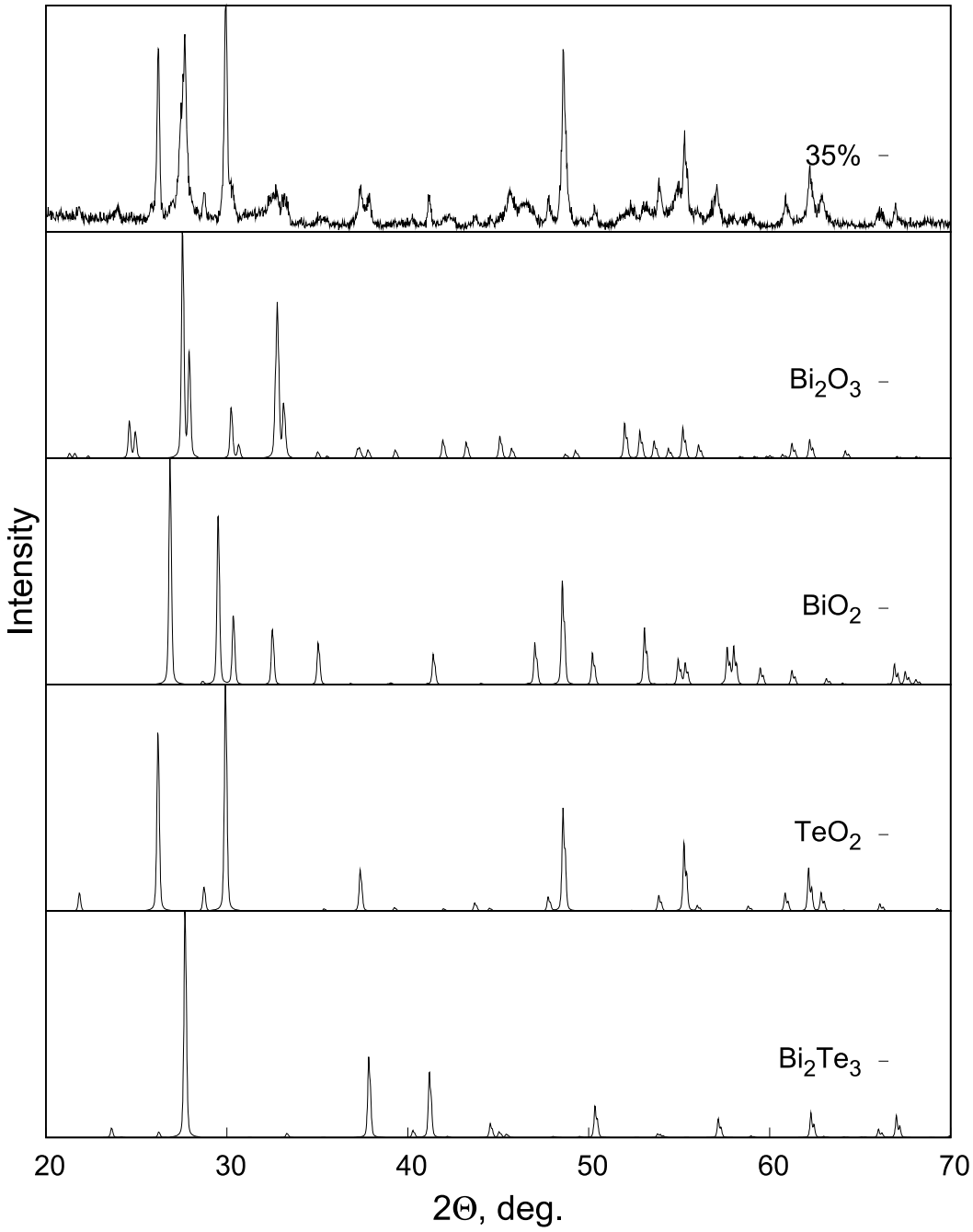

Fig S25. XRD pattern of the ,material after 35% of the reaction

Reference data from Powder Diffraction File:
Bi_2O_3: 00-050-1088_11
BiO_2: 01-083-0410_14
TeO_2: 01-078-1713_10
Bi2Te3: 01-079-4904_9

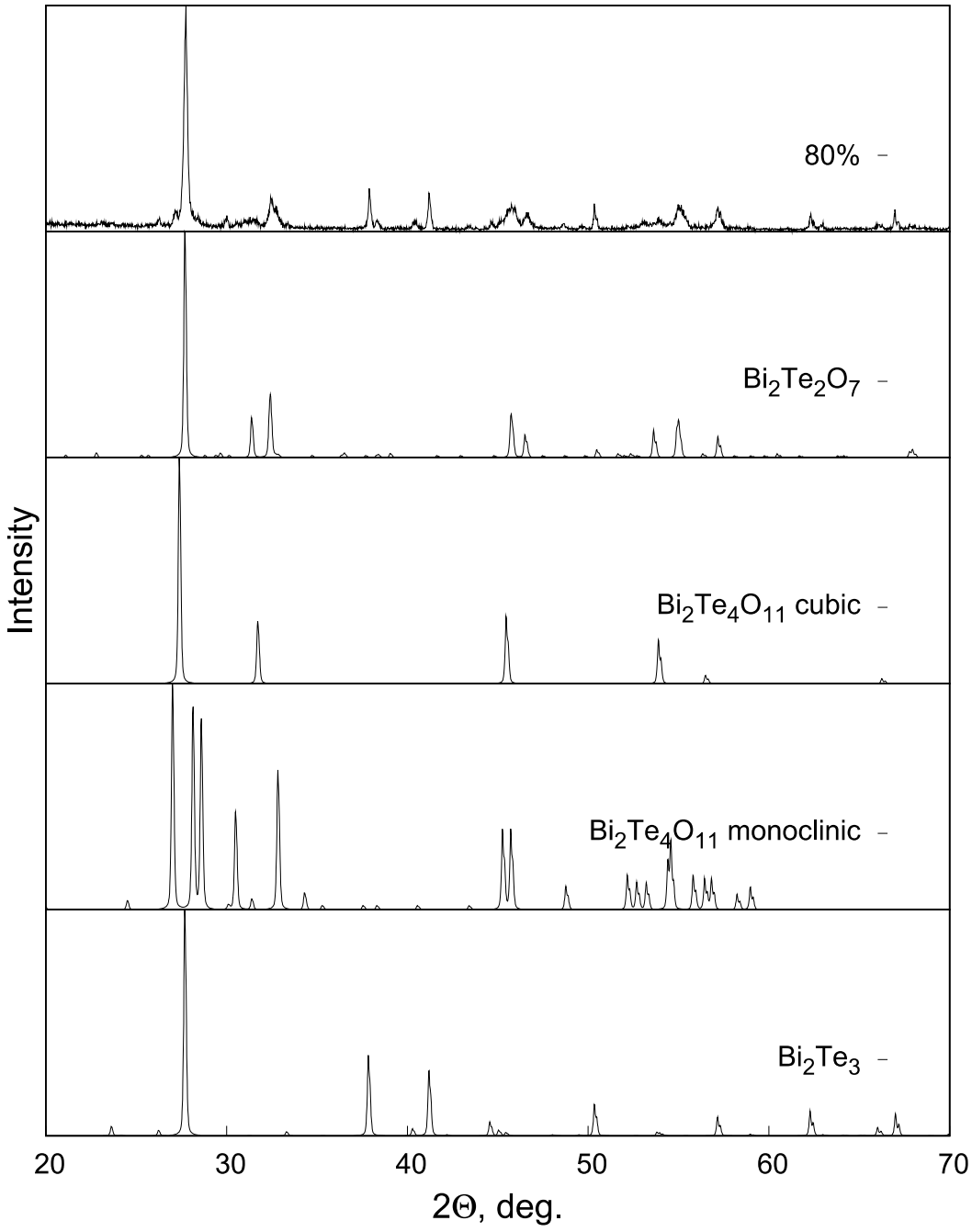

Fig S26. XRD pattern of the material after 80% of the reaction

Reference data from Powder Diffraction File:
$Bi_2Te_2O_7$: 00-052-1260_19
$Bi_2Te_4O_{11}$ cubic: 01-089-4588_20
$Bi_2Te_4O_{11}$ monoclinic: 00-026-0227_21
Bi_2Te_3: 01-079-4904_9

$Bi_2Te_3O_x$ stands for the mixture of $Bi_2Te_2O_7$ and $Bi_2Te_4O_{11}$

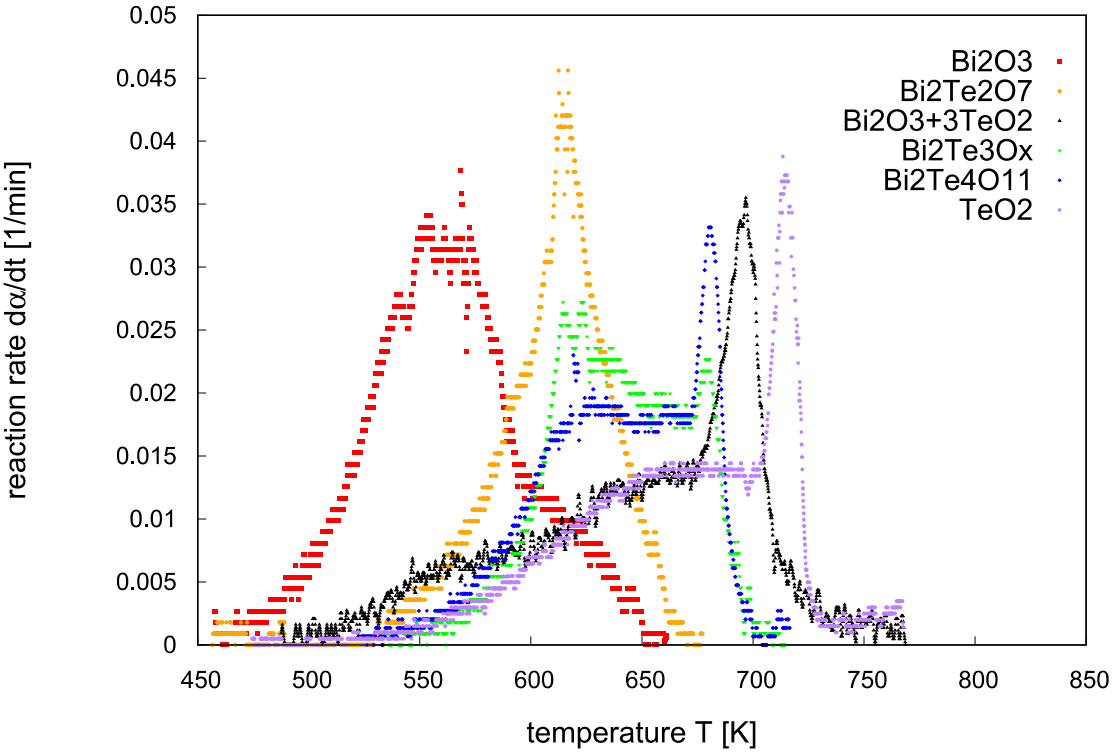

Fig. S27. Comparison of the rates of different reactions for 2 K/min heating rate.

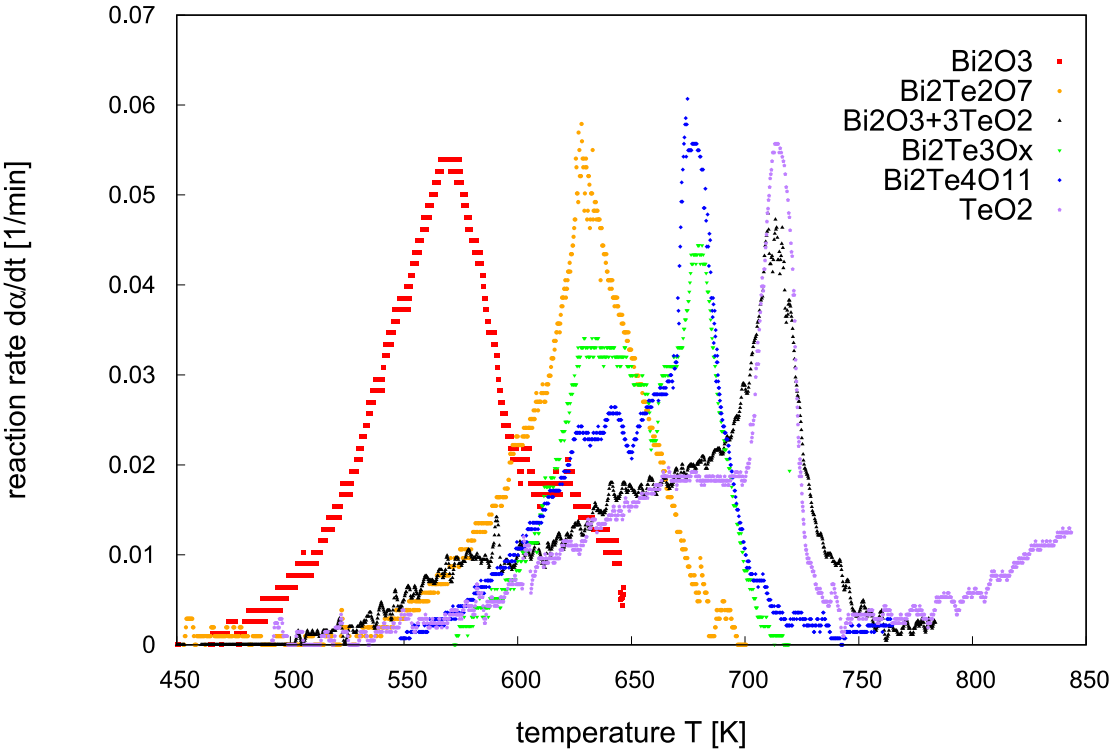

Fig. S28. Comparison of the rates of different reactions for 3 K/min heating rate.

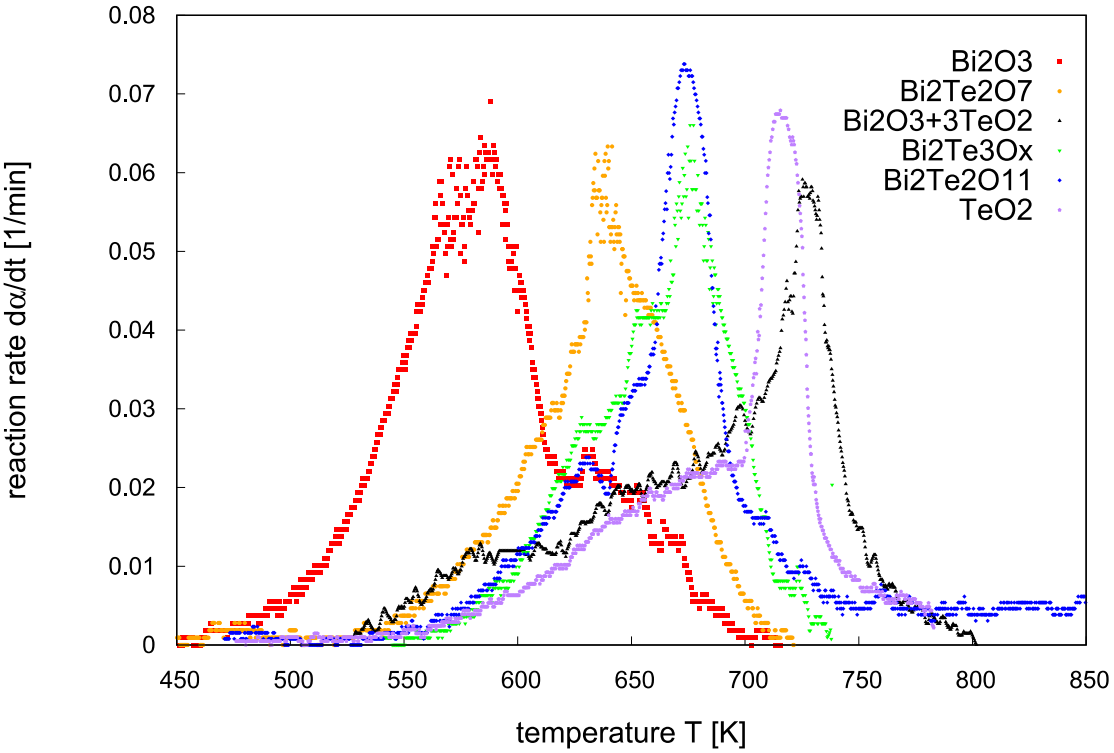

Fig. S29. Comparison of the rates of different reactions for 4 K/min heating rate.

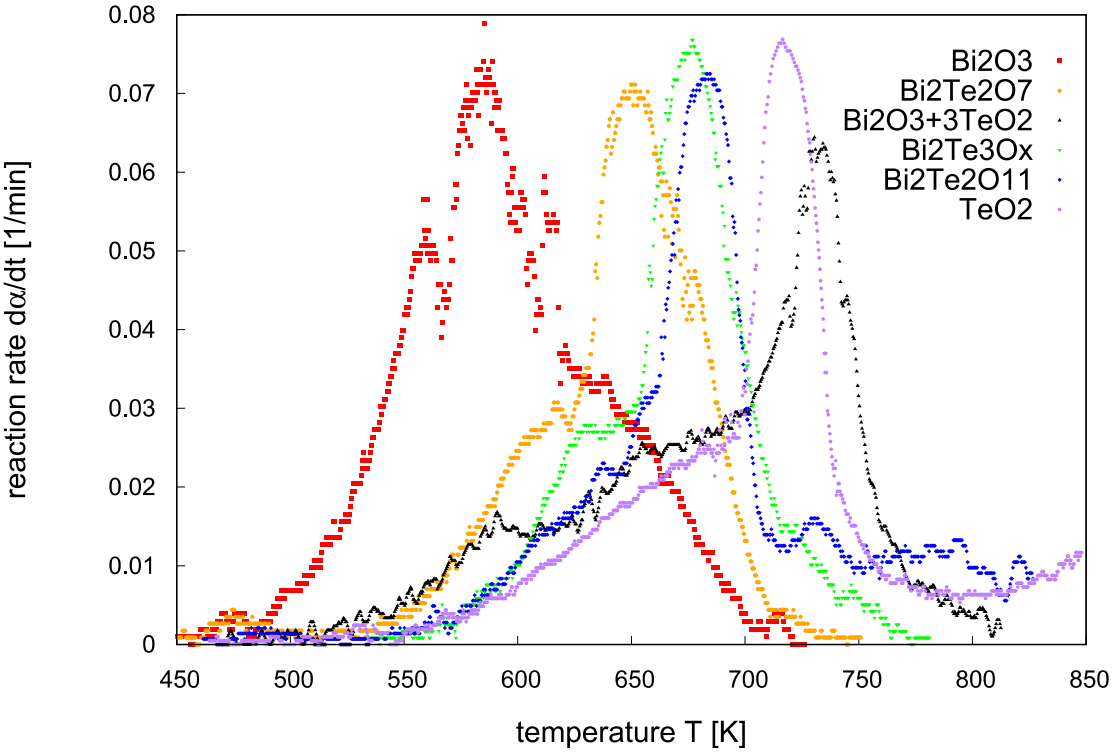

Fig. S30. Comparison of the rates of different reactions for 5 K/min heating rate.

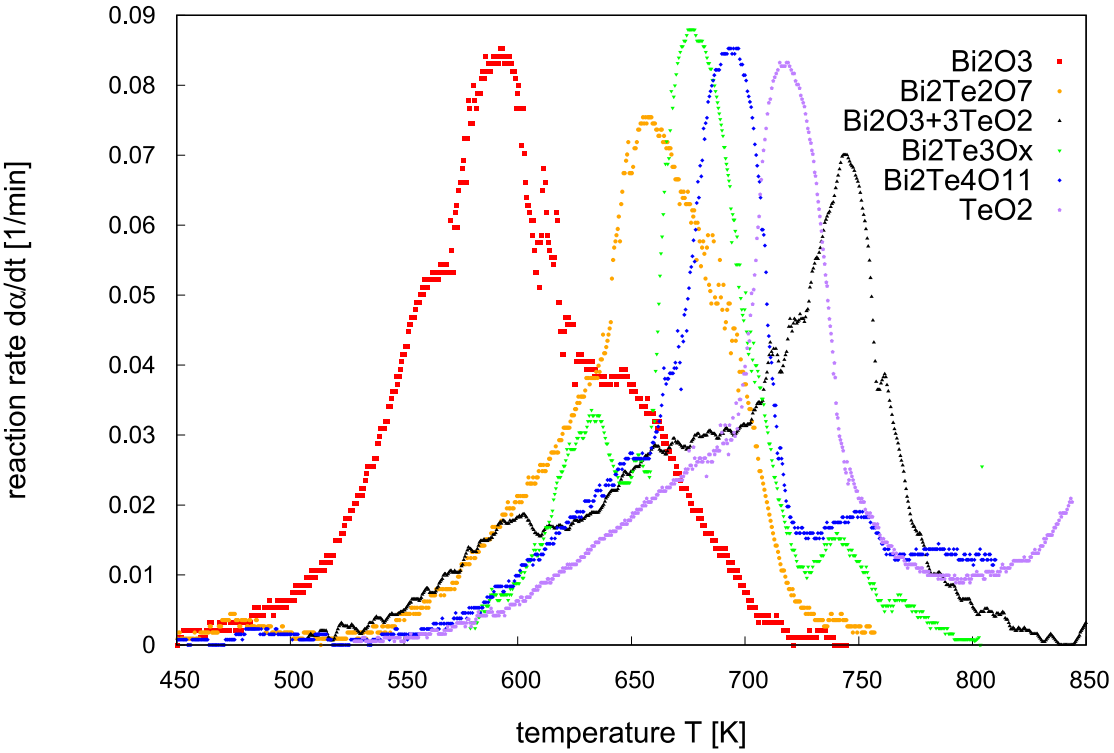

Fig. S31. Comparison of the rates of different reactions for 6 K/min heating rate.

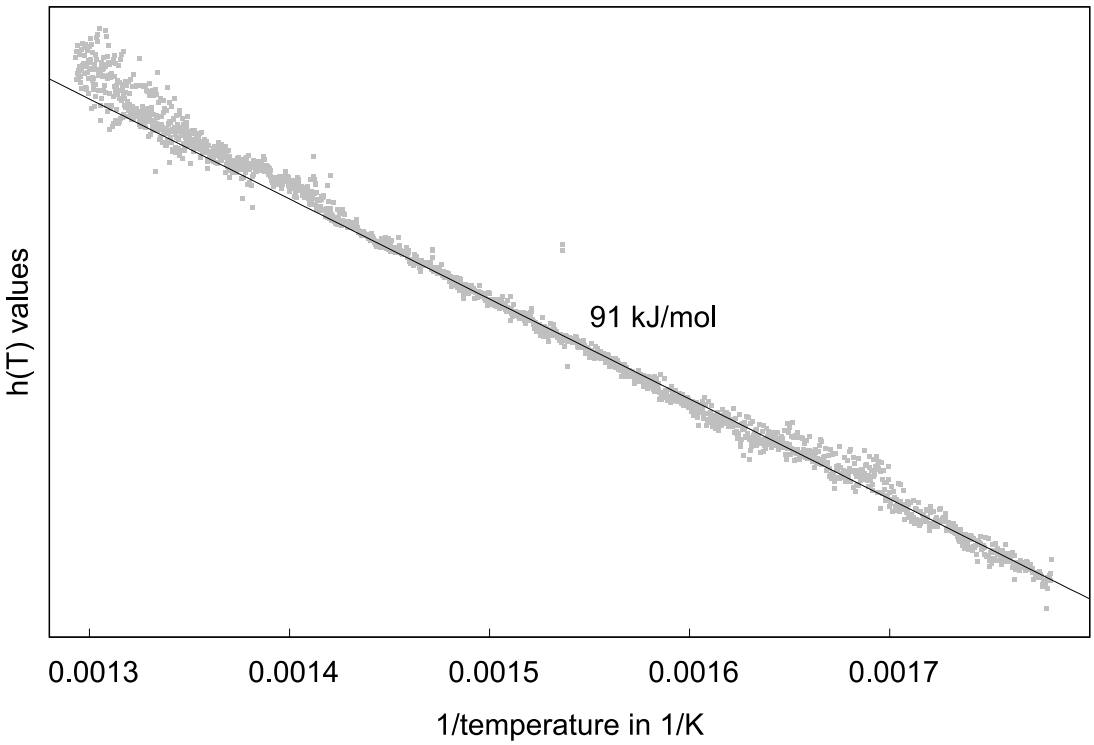

Fig. S32. Thermal function h(T) obtained from non-parametric analysis of the mixed oxides reaction data